Eur. Phys. J. E (2014) **37**: 33
DOI 10.1140/epje/i2014-14033-2

THE EUROPEAN PHYSICAL JOURNAL E

Regular Article

Collapsed heteroclinic snaking near a heteroclinic chain in dragged meniscus problems*

D. Tseluiko[1,a], M. Galvagno[1,a,b], and U. Thiele[2]

[1] Department of Mathematical Sciences, Loughborough University, Leicestershire, LE11 3TU, UK
[2] Institut für Theoretische Physik, Westfälische Wilhelms-Universität Münster, Wilhelm Klemm Str. 9, D-48149 Münster, Germany

Received 16 July 2013 and Received in final form 20 December 2013
Published online: 28 April 2014 –

Abstract. A liquid film is studied that is deposited onto a flat plate that is inclined at a constant angle to the horizontal and is extracted from a liquid bath at a constant speed. We analyse steady-state solutions of a long-wave evolution equation for the film thickness. Using centre manifold theory, we first obtain an asymptotic expansion of solutions in the bath region. The presence of an additional temperature gradient along the plate that induces a Marangoni shear stress significantly changes these expansions and leads to the presence of logarithmic terms that are absent otherwise. Next, we numerically obtain steady solutions and analyse their behaviour as the plate velocity is changed. We observe that the bifurcation curve exhibits collapsed (or exponential) heteroclinic snaking when the plate inclination angle is above a certain critical value. Otherwise, the bifurcation curve is monotonic. The steady profiles along these curves are characterised by a foot-like structure that is formed close to the meniscus and is preceded by a thin precursor film further up the plate. The length of the foot increases along the bifurcation curve. Finally, we prove with a Shilnikov-type method that the snaking behaviour of the bifurcation curves is caused by the existence of an infinite number of heteroclinic orbits close to a heteroclinic chain that connects in an appropriate three-dimensional phase space the fixed point corresponding to the precursor film with the fixed point corresponding to the foot and then with the fixed point corresponding to the bath.

1 Introduction

Spreading liquids on a surface by pulling a plate out of a liquid bath is a well known coating process used for industrial applications [1]. In order to gain control over the coating process, this problem has been studied from an experimental point of view, see, *e.g.*, refs. [2–7], and also theoretically, see, *e.g.*, refs. [5,8–12]. Landau and Levich [8], for example, analysed liquid films of constant thickness coating a vertical plate extracted from a bath of liquid at low velocities and found that the film thickness scales as $U^{2/3}$, where U is the velocity of the plate. The asymptotic result of Landau and Levich was improved by Wilson [11]. Non-Landau-Levich-type solutions, which satisfy other scaling laws, were also found, see, for example, refs. [5,13–16]. In particular, multiple non-Landau-Levich type solutions were previously observed by Münch *et al.* [16] for certain parameter values in a similar system, where the role of the plate withdrawal is taken by a Marangoni shearing induced by a constant temperature gradient on the plate. Related behaviour is also found in coating problems involving complex fluids. A particular example is the deposition of line patterns in the process of Langmuir-Blodgett transfer of a surfactant layer from a bath onto a moving plate [17,18]. For this system a reduced Cahn-Hilliard type model was employed to show that the deposition of lines is related to local and global bifurcations of time-periodic states from a snaking bifurcation curve of steady-state front solutions [19], that in the light of the present work may be seen as a case of heteroclinic snaking (also cf. review [20] where this is set into the wider context of deposition patterns).

In the present study, we do not consider Landau-Levich solutions where the thick drawn film directly connects to the meniscus of the bath. Instead we focus on a different type of thickness profiles which show a foot-like structure of characteristic thickness h_f close to the meniscus that is preceded by a very thin precursor film of characteristic thickness h_p further up the plate. They were recently described for a slip model [5,12]. We show that for the precursor film model (as known in case of the slip model) at inclination angles α below a critical value α_c, the foot

* Contribution to the Topical Issue "Irreversible Dynamics: A topical issue dedicated to Paul Manneville" edited by Patrice Le Gal and Laurette S. Tuckerman.

[a] These authors have equally contributed to this work.
[b] e-mail: m.galvagno2@lboro.ac.uk

Table 1. Hierarchy of systems exhibiting collapsed (or exponential) snaking behaviour.

Authors	Description of scenario	# fixed points
Shilnikov [21] Glendinning and Sparrow [22]	Infinite number of periodic orbits approaching a homocline	1 fixed point
J. Knobloch and Wagenknecht [23] Ma, Burke and E. Knobloch [24]	Infinite number of homoclines approaching a hetereoclinic cycle	2 fixed points
Present study	Infinite number of heteroclines approaching a hetereoclinic chain	3 fixed points

shape is monotonic while for $\alpha > \alpha_c$ there exist undulations on top of the foot. In both cases we observe that for each inclination angle foot solutions exist when the plate velocity is close to a certain limiting velocity, and the closer the bifurcation curve approaches this limiting value, the larger the foot length becomes. The analysis of the bifurcation diagrams of foot solutions for a suitable solution measure, shows that this classical physico-chemical problem turns out to be a rich example to illustrate collapsed (or exponential) heteroclinic snaking near a hetereoclinic chain[1]. We demonstrate that the three regions of the liquid film profile, namely, the precursor film, the foot and the bath, can be considered as three fixed points $\boldsymbol{y}_p$, $\boldsymbol{y}_f$ and $\boldsymbol{y}_b$ of an appropriate three-dimensional dynamical system. The steady film profiles are then described by heteroclinic orbits connecting points $\boldsymbol{y}_p$ and $\boldsymbol{y}_b$. Then, we show that the collapsed heteroclinic snaking observed in the dragged meniscus problem is caused by a perturbation of a heteroclinic chain that connects $\boldsymbol{y}_p$ with $\boldsymbol{y}_f$ and $\boldsymbol{y}_f$ with $\boldsymbol{y}_b$ that exists for certain parameter values, provided that fixed points $\boldsymbol{y}_p$ and $\boldsymbol{y}_b$ have two-dimensional unstable and two-dimensional stable manifolds, respectively, and that the fixed point $\boldsymbol{y}_f$ is a saddle focus with a one-dimensional stable manifold and a two-dimensional unstable manifold.

Note that related collapsed snaking behaviour has been analysed in systems involving either one fixed point [21, 25,22] or two fixed points [23,24]. Table 1 illustrates that our results form part of a hierarchy of such snaking behaviours: Shilnikov (see refs. [21,25]) analyses homoclinic orbits to saddle-focus fixed points in three-dimensional dynamical systems that exist for some value β_0 of a parameter β and demonstrates that if the fixed point has a one-dimensional unstable manifold and a two-dimensional stable manifold, so that the eigenvalues of the Jacobian at this point are λ_1 and $-\lambda_2 \pm \mathrm{i}\,\omega$, where $\lambda_{1,2}$ and ω are positive real numbers, and if the saddle index $\delta \equiv \lambda_2/\lambda_1 < 1$, then in the neighbourhood of the primary homoclinic orbit there exists an infinite number of periodic orbits that pass near the fixed point several times. Moreover, the difference in the periods of these orbit tends asymptotically to π/ω. The perturbation of the structurally unstable homoclinic orbit leads to a snaking bifurcation diagram showing the dependence of the period of the orbit *versus* the bifurcation parameter β. This diagram has an infinite but countable number of turning points at which the periodic orbits vanish in saddle-node bifurcations. However, if the saddle index is greater than unity, then the bifurcation diagram is monotonic. Knobloch and Wagenknecht [23,26] analyse symmetric heteroclinic cycles connecting saddle-focus equilibria in reversible four-dimensional dynamical systems that arise in a number of applications, *e.g.*, in models for water waves in horizontal channels [27] and in the study of cellular buckling in structural mechanics [28]. In these systems the symmetric heteroclinic cycle organises the dynamics in an equivalent way to the homoclinic solution in Shilnikov's case. It is found that a necessary condition for collapsed snaking in such four-dimensional systems is the requirement that one of the involved fixed points is a bi-focus [23]. Then there exists an infinite number of homoclines to the second involved fixed point that all pass a close neighbourhood of the bi-focus. The presently studied case is equivalent to the cases of Shilnikov and of Knobloch and Wagenknecht, however, here a heteroclinic chain between three fixed points forms the organising centre of an infinite number of heteroclines.

The rest of the paper is organised as follows. In sect. 2, we introduce the model equation. In sect. 3, we analyse asymptotic behaviour of solutions in the bath region. In sect. 4 we present numerical results for the steady states and their snaking behaviour in the cases without and with Marangoni driving. Section 5 is devoted to an analytical explanation of the bifurcation diagrams obtained in sect. 4. Finally, in sect. 6 we present our conclusions.

2 Model equation

We consider a flat plate that forms a constant angle with the horizontal direction and that is being withdrawn from a pool of liquid at a constant speed. A schematic representation of the system is shown in fig. 1. We introduce a Cartesian coordinate system (x, z) with the x-axis pointing downwards along the plate and the z-axis pointing upwards and being perpendicular to the plate. We assume that the free surface is two-dimensional, with no variations in the transverse direction. The position of the free surface is given by the equation $z = h(x, t)$, where t denotes time. As a model equation governing the evolution of the free surface, we use a long-wave equation derived in refs. [29,

[1] We introduce the term "collapsed heteroclinic snaking" to indicate that the corresponding bifurcation diagram consists of a snaking curve of heteroclinic orbits that is collapsed (exponentially decreasing snaking amplitude) in the sense used in ref. [24] for homoclinic orbits close to a heteroclinic chain that connects two fixed points in a reversible system.

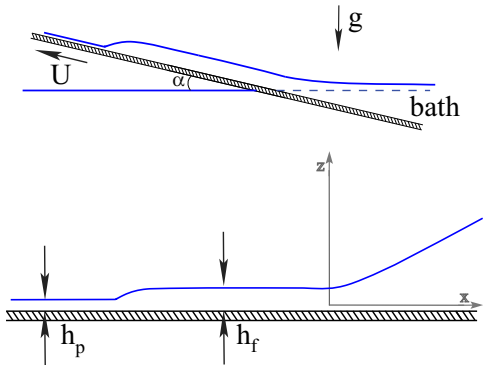

Fig. 1. Sketch of the problem: Upper panel: An infinitely extended flat plate inclined at an angle α is withdrawn at a constant speed U from a bath of a partially wetting liquid. Lower panel: Definition of the precursor film height, h_p, and the foot film height, h_f, for a typical film profile.

30] from the Navier-Stokes equations and the corresponding boundary conditions under the assumptions that the physical plate inclination angle is small and the typical longitudinal length scale of free-surface variations is large compared to the typical film thickness:

$$\partial_t h = -\partial_x \Big(\frac{h^3}{3} \partial_x [\partial_x^2 h + \Pi(h)] - \frac{h^3}{3} G(\partial_x h - \alpha) - \frac{U}{3} h \Big). \tag{1}$$

Here α, U and G are the scaled inclination angle of the plate, the scaled plate velocity and the scaled gravity, respectively, and the symbols ∂_t and ∂_x denote partial differentiation with respect to t and x, respectively. Note that the scaled angle α as well as the scaled equilibrium contact angle are $O(1)$ quantities. On the right-hand side, $-\partial_x^2 h$ represents the Laplace pressure, $\Pi(h)$ represents the Derjaguin or disjoining pressure (that we will discuss in detail below), the term $G\partial_x h$ is due to the hydrostatic-pressure, $-G\alpha$ is due to the x-component of gravity and the last term is due to the drag of the plate.

The interaction between the plate and the non-volatile partially wetting liquid is modelled via the disjoining pressure, which has the dimensional form

$$\widetilde{\Pi}(\tilde{h}) = \widetilde{\Pi}_1(\tilde{h}) + \widetilde{\Pi}_2(\tilde{h}) = -\frac{A}{\tilde{h}^3} + \frac{B}{\tilde{h}^6} \tag{2}$$

consisting of a destabilising long-range van der Waals interaction, $\widetilde{\Pi}_1(\tilde{h}) = -A/\tilde{h}^3$, and a stabilising short-range interaction, $\widetilde{\Pi}_2(\tilde{h}) = B/\tilde{h}^6$. Here $\tilde{h}$ is the dimensional film thickness, and A and B are the Hamaker constants. For A and B positive, on a horizontal plane the disjoining pressure describes partial wetting and characterises a stable precursor film of thickness

$$h_{\rm eq} = (B/A)^{1/3} \tag{3}$$

that may coexist with a meniscus of finite contact angle

$$\theta_{\rm eq} = \sqrt{\frac{3}{5} \frac{A}{\gamma h_{\rm eq}^2}}, \tag{4}$$

where γ is the surface tension coefficient (see refs. [30–33] for background information and details).

Equation (1) has been non-dimensionalised using $\ell = \sqrt{3/5}\, h_{\rm eq}/\theta_{\rm eq}$ as the length scale in the x-direction, $h_{\rm eq}$ as the length scale in the z-direction and $\tau{=}(9\eta h_{\rm eq})/(25\gamma\theta_{\rm eq}^4)$ as the time scale, where η is the viscosity of the liquid. Note that with this non-dimensionalisation the dimensionless disjoining pressure has the form

$$\Pi(h) = \Pi_1(h) + \Pi_2(h) = -\frac{1}{h^3} + \frac{1}{h^6}. \tag{5}$$

The scaled velocity, gravity number and the inclination angle are given by

$$U = \frac{3\tau}{\ell} u, \quad G = \frac{\rho g h_{\rm eq}^4}{A}, \quad \alpha = \frac{\ell}{h_{\rm eq}} \tilde{\alpha}, \tag{6}$$

respectively, where ρ is the density of the liquid and g is gravity and u and $\tilde{\alpha}$ are the dimensional plate velocity and the small physical plate inclination angle, respectively.

Note that additional physical effects can be included into the model presented above. One extension that is interesting for reasons that will become clear later, is the inclusion of a term quadratic in h in the flux on the right-hand side of eq. (1). This can be obtained, for example, by assuming that there is an additional constant temperature gradient along the plate, see refs. [16,34–36] for more details. Inclusion of this effect into the present model results in

$$\partial_t h = -\partial_x \Big(\frac{h^3}{3} \partial_x [\partial_x^2 h + \Pi(h)] - \frac{h^3}{3} G(\partial_x h - \alpha) - \frac{\Omega}{3} h^2 - \frac{U}{3} h \Big), \tag{7}$$

where Ω is a dimensionless number representing the temperature gradient along the plate.

Finally, we discuss boundary conditions. First, we assume that h tends to an undetermined constant value (*e.g.*, at equilibrium the precursor film thickness) as $x \to -\infty$ and its derivatives tend to zero as $x \to -\infty$. Second, we assume that $h_x = \alpha + o(1)$ as $x \to \infty$, which means that the slope of the free surface of the bath approaches the horizontal direction far away from the plate. The asymptotic behaviour of h as $x \to \infty$ will be analysed in more detail in the next section.

3 Asymptotic behaviour of solutions at infinity

In what follows, we will analyse steady-state solutions of eq. (7), *i.e.*, solutions that satisfy the equation

$$h^3[h'' + \Pi(h)]' - Gh^3(h' - \alpha) - \Omega h^2 - Uh + C_0 = 0, \tag{8}$$

where now h is a function of x only and primes denote differentiation with respect to x. Here, C_0 is a constant of integration and represents the flux. Note that C_0 is in fact not an independent parameter but is determined as part of the solution of the boundary-value problem consisting of eq. (8) and four boundary conditions that will be discussed in the next section.

Following a proposal of ref. [16], we introduce variables $y_1 = 1/h$, $y_2 = h'$ and $y_3 = h''$, and convert the steady-state equation (8) into a three-dimensional dynamical system

$$y_1' = -y_1^2 y_2, \tag{9}$$

$$y_2' = y_3, \tag{10}$$

$$y_3' = (6y_1^7 - 3y_1^4)y_2 + Gy_2 + Uy_1^2 + \Omega y_1 - C_0 y_1^3 - G\alpha. \tag{11}$$

Note that the transformation $y_1 = 1/h$ is used to obtain a new fixed point corresponding to the bath, namely the point $\boldsymbol{y}_b = (0, \alpha, 0)$, beside other fixed points, two of which, $\boldsymbol{y}_f = (1/h_f, 0, 0)$ and $\boldsymbol{y}_p = (1/h_p, 0, 0)$, correspond to the foot and the precursor film, respectively. For a more detailed analysis of the fixed points, see the beginning of sect. 5.

To analyse the stability of the fixed point $\boldsymbol{y}_b$, we first compute the Jacobian at this point:

$$\boldsymbol{J}_{\boldsymbol{y}_b} = \begin{pmatrix} 0 & 0 & 0 \\ 0 & 0 & 1 \\ \Omega & G & 0 \end{pmatrix}. \tag{12}$$

The eigenvalues are 0, $\pm G^{1/2}$ and the corresponding eigenvectors are $(G, -\Omega, 0)$, $(0, \pm G^{-1/2}, 1)$. So there is a one-dimensional centre (or critical) eigenspace, a one-dimensional stable eigenspace and a one-dimensional unstable eigenspace given by

$$T^c_{\boldsymbol{y}_b} = \mathrm{span}\{(G, -\Omega, 0)\}, \tag{13}$$

$$T^s_{\boldsymbol{y}_b} = \mathrm{span}\{(0, -G^{-1/2}, 1)\}, \tag{14}$$

$$T^u_{\boldsymbol{y}_b} = \mathrm{span}\{(0, G^{-1/2}, 1)\}, \tag{15}$$

respectively.

To determine the asymptotic behaviour of h as $x \to \infty$, we analyse the centre manifold of $\boldsymbol{y}_b$, which we denote by $W^c_{\boldsymbol{y}_b}$. This is an invariant manifold whose tangent space at $\boldsymbol{y}_b$ is $T^c_{\boldsymbol{y}_b}$. The existence of a centre manifold is provided by the centre manifold theorem (see, *e.g.*, theorem 1, p. 4 in ref. [37], theorem 5.1, p. 152 in ref. [38]). For simplicity, we use the substitution $z_1 = y_1$, $z_2 = y_2 - \alpha$, $z_3 = y_3$. In vector notation, the dynamical system takes the form

$$\boldsymbol{z}' = \boldsymbol{f}(\boldsymbol{z}), \tag{16}$$

where $\boldsymbol{f}(\boldsymbol{z}) = (f_1(\boldsymbol{z}), f_2(\boldsymbol{z}), f_3(\boldsymbol{z}))^T$ and

$$f_1(\boldsymbol{z}) = f_1(z_1, z_2, z_3) = -z_1^2(z_2 + \alpha), \tag{17}$$

$$f_2(\boldsymbol{z}) = f_2(z_1, z_2, z_3) = z_3, \tag{18}$$

$$f_3(\boldsymbol{z}) = f_3(z_1, z_2, z_3) = (6z_1^7 - 3z_1^4)(z_2 + \alpha) + Gz_2 + Uz_1^2 + \Omega z_1 - C_0 z_1^3. \tag{19}$$

The fixed point corresponding to the bath is then $\boldsymbol{z}_b = (0, 0, 0)$. Next, we rewrite the system of ordinary differential equations (16) in its eigenbasis at $\boldsymbol{z}_b$, *i.e.*, we use the change of variables $\boldsymbol{u} = \boldsymbol{B}^{-1}\boldsymbol{z}$, where $\boldsymbol{B}$ is the matrix having the eigenvectors of the Jacobian as its columns,

$$\boldsymbol{B} = \begin{pmatrix} G & 0 & 0 \\ -\Omega & G^{-1/2} & -G^{-1/2} \\ 0 & 1 & 1 \end{pmatrix}, \tag{20}$$

and obtain the system

$$\boldsymbol{u}' = \boldsymbol{g}(\boldsymbol{u}) \equiv \boldsymbol{B}^{-1}\boldsymbol{f}(\boldsymbol{B}\boldsymbol{u}), \tag{21}$$

which can be written in the form

$$\xi' = \psi(\xi, \boldsymbol{\eta}), \tag{22}$$

$$\boldsymbol{\eta}' = \boldsymbol{C}\boldsymbol{\eta} + \boldsymbol{\varphi}(\xi, \boldsymbol{\eta}), \tag{23}$$

where ξ denotes the first component of $\boldsymbol{u}$ and $\boldsymbol{\eta} = (\eta_1, \eta_2)^T$ consist of the second and the third components of $\boldsymbol{u}$ (*i.e.*, $\xi \equiv u_1$, $\eta_1 \equiv u_2$ and $\eta_2 \equiv u_3$), ψ and $\boldsymbol{\varphi}$ have Taylor expansions that start with quadratic or even higher order terms and $\boldsymbol{C}$ is the matrix

$$\boldsymbol{C} = \begin{pmatrix} G^{1/2} & 0 \\ 0 & -G^{1/2} \end{pmatrix}. \tag{24}$$

After some algebra, we find

$$\psi(\xi, \boldsymbol{\eta}) = G\Omega\xi^3 - G\alpha\xi^2 - G^{1/2}\xi^2\eta_1 + G^{1/2}\xi^2\eta_2, \tag{25}$$

$$\begin{aligned}\varphi_1(\xi, \boldsymbol{\eta}) = {} & -3\,G^7\,\Omega\,\xi^8 + 3\,G^7\alpha\,\xi^7 + 3\,G^{13/2}\xi^7\eta_1 \\ & -3\,G^{13/2}\xi^7\eta_2 + \frac{3}{2}\,G^4\Omega\,\xi^5 - \frac{3}{2}\,G^4\alpha\,\xi^4 \\ & -\frac{3}{2}\,G^{7/2}\xi^4\eta_1 + \frac{3}{2}\,G^{7/2}\xi^4\eta_2 - \frac{1}{2}\,C_0\,G^3\xi^3 \\ & +\frac{1}{2}\,G^{3/2}\Omega^2\xi^3 - \frac{1}{2}\,G^{3/2}\Omega\,\alpha\,\xi^2 + \frac{1}{2}\,UG^2\xi^2 \\ & -\frac{1}{2}\,G\Omega\,\xi^2\eta_1 + \frac{1}{2}\,G\Omega\,\xi^2\eta_2,\end{aligned} \tag{26}$$

$$\begin{aligned}\varphi_2(\xi, \boldsymbol{\eta}) = {} & -G^{1/2}\eta_2 - 3\,G^7\,\Omega\,\xi^8 + 3\,G^7\alpha\,\xi^7 \\ & +3\,G^{13/2}\xi^7\eta_1 - 3\,G^{13/2}\xi^7\eta_2 + \frac{3}{2}\,G^4\Omega\,\xi^5 \\ & -\frac{3}{2}\,G^4\alpha\,\xi^4 - \frac{3}{2}\,G^{7/2}\xi^4\eta_1 + \frac{3}{2}\,G^{7/2}\xi^4\eta_2 \\ & -\frac{1}{2}\,C_0\,G^3\xi^3 - \frac{1}{2}\,G^{3/2}\Omega^2\xi^3 + \frac{1}{2}\,G^{3/2}\Omega\,\alpha\,\xi^2 \\ & +\frac{1}{2}\,UG^2\xi^2 + \frac{1}{2}\,G\Omega\,\xi^2\eta_1 - \frac{1}{2}\,G\Omega\,\xi^2\eta_2.\end{aligned} \tag{27}$$

Near the origin, $\boldsymbol{z}_b$, when $|\xi| < \delta$ for some positive δ, the centre manifold in the (ξ, η_1, η_2)-space can be represented by the equations $\eta_1 = g_1(\xi)$, $\eta_2 = g_2(\xi)$, where g_1 and g_2 are in C^2. Moreover, near the origin system (22), (23) is topologically equivalent to the system

$$\xi' = \psi(\xi, \boldsymbol{g}(\xi)), \tag{28}$$

$$\boldsymbol{\eta}' = \boldsymbol{C}\boldsymbol{\eta}, \tag{29}$$

where the first equation represents the restriction of the flow to its centre manifold (see, *e.g.*, theorem 1, p. 4 in ref. [37], theorem 5.2, p. 155 in ref. [38]).

The centre manifold can be approximated to any degree of accuracy. According to theorem 3, p. 5 in ref. [37], "test" functions ϕ_1 and ϕ_2 approximate the centre manifold with accuracy $O(|\xi|^q)$, namely

$$|g_1(\xi)-\phi_1(\xi)| = O(|\xi|^q), \quad |g_2(\xi)-\phi_2(\xi)| = O(|\xi|^q) \quad (30)$$

as $\xi \to 0$, provided that $\phi_i(0) = 0$, $\phi_i'(0) = 0$, $i = 1, 2$ and $\boldsymbol{M}[\boldsymbol{\phi}](\xi) = O(|\xi|^q)$ as $\xi \to 0$, where $\boldsymbol{M}$ is the operator defined by

$$\boldsymbol{M}[\boldsymbol{\phi}](\xi) = \boldsymbol{\phi}'(\xi)\psi(\xi, \boldsymbol{\phi}(\xi)) - \boldsymbol{C}\boldsymbol{\phi}(\xi) - \boldsymbol{\varphi}(\xi, \boldsymbol{\phi}(\xi)). \quad (31)$$

The centre manifold can now be obtained by seeking for $\phi_1(\xi)$ and $\phi_2(\xi)$ in the form of polynomials in ξ and requiring that the coefficients of the expansion of $\boldsymbol{M}[\boldsymbol{\phi}](\xi)$ in Taylor series vanish at zeroth order, first order, second order, etc. Using this procedure, we can find the Taylor series expansions of g_1 and g_2

$$\begin{aligned} g_1(\xi)=&\left(\frac{1}{2}\,G\Omega\,\alpha - \frac{1}{2}\,G^{3/2}U\right)\xi^2 \\ &+\left(G^2U\alpha - G^{3/2}\Omega\,\alpha^2 - \frac{1}{2}\,G\Omega^2 + \frac{1}{2}\,G^{5/2}C_0\right)\xi^3 \\ &-\left(\frac{3}{2}\,G^3\alpha\,C_0 - 3\,G^2\alpha^3\Omega + \frac{3}{2}\,G^2\Omega\,U - 3\,G^{5/2}\alpha^2U\right. \\ &\left.-\frac{3}{2}\,G^{7/2}\alpha - \frac{5}{2}\,G^{3/2}\alpha\,\Omega^2\right)\xi^4 + \cdots, \end{aligned} \quad (32)$$

$$\begin{aligned} g_2(\xi)=&\left(\frac{1}{2}\,G\Omega\,\alpha + \frac{1}{2}\,G^{3/2}U\right)\xi^2 \\ &+\left(G^2U\alpha + G^{3/2}\Omega\,\alpha^2 - \frac{1}{2}\,G\Omega^2 - \frac{1}{2}\,G^{5/2}C_0\right)\xi^3 \\ &-\left(\frac{3}{2}\,G^3\alpha\,C_0 - 3\,G^2\alpha^3\Omega - 3\,G^{5/2}\alpha^2U + \frac{3}{2}\,G^2\Omega\,U\right. \\ &\left.+\frac{3}{2}\,G^{7/2}\alpha + \frac{5}{2}\,G^{3/2}\alpha\,\Omega^2\right)\xi^4 + \cdots. \end{aligned} \quad (33)$$

Let $g_i^{(k)}(\xi)$, $i = 1, 2$, be the Taylor polynomial for $g_i(\xi)$ of degree k. Then $g_i(\xi) = g_i^{(k)}(\xi) + O(|\xi|^{k+1})$, $i = 1, 2$, and $\boldsymbol{M}[\boldsymbol{g}^{(k)}](\xi) = O(|\xi|^{k+1})$ as $\xi \to 0$. The dynamics on the centre manifold is therefore governed by the equation

$$\begin{aligned} \xi' &= \psi(\xi, \boldsymbol{g}^{(k)}(\xi)) + O(|\xi|^{k+3}) \\ &= G\Omega\xi^3 - G\alpha\xi^2 - G^{1/2}\xi^2 g_1^{(k)}(\xi) \\ &\quad +G^{1/2}\xi^2 g_2^{(k)}(\xi) + O(|\xi|^{k+3}). \end{aligned} \quad (34)$$

Substituting eq. (32) and eq. (33) into eq. (34), we find

$$\begin{aligned} \xi' = &-G\alpha\xi^2 + G\Omega\xi^3 + UG^2\xi^4 - (C_0G^3 - 2G^2\Omega\alpha^2)\xi^5 \\ &+(6G^3U\alpha^2 - 3G^4\alpha - 5G^2\Omega^2\alpha)\xi^6 + \cdots. \end{aligned} \quad (35)$$

Taking into account the fact that $\xi = z_1/G$, we obtain

$$\begin{aligned} z_1' = &-\alpha z_1^2 + \frac{\Omega}{G}z_1^3 + \frac{U}{G}z_1^4 - \left(\frac{C_0}{G} - \frac{2\Omega\alpha^2}{G^2}\right)z_1^5 \\ &+\left(\frac{6U\alpha^2}{G^2} - \frac{3\alpha}{G} - \frac{5\Omega^2\alpha}{G^3}\right)z_1^6 + \cdots. \end{aligned} \quad (36)$$

Rewriting this in terms of h, we get

$$\begin{aligned} h' = &\alpha - \frac{\Omega}{G}h^{-1} - \frac{U}{G}h^{-2} + \left(\frac{C_0}{G} - \frac{2\Omega\alpha^2}{G^2}\right)h^{-3} \\ &-\left(\frac{6U\alpha^2}{G^2} - \frac{3\alpha}{G} - \frac{5\Omega^2\alpha}{G^3}\right)h^{-4} + \cdots \end{aligned} \quad (37)$$

as $h \to \infty$.

We seek for a solution for h whose slope approaches that of the line corresponding to the horizontal direction as $x \to \infty$. In the chosen system of coordinates, the line corresponding to the horizontal direction has the slope α. So we seek for a solution satisfying $h'(x) = \alpha + o(1)$ as $x \to \infty$. This can also be written in the form

$$h(x) = \alpha x + o(x) \quad \text{as} \quad x \to \infty. \quad (38)$$

Substituting eq. (38) into eq. (37), we obtain

$$h' = \alpha - \frac{\Omega}{\alpha G}x^{-1} + o(x^{-1}), \quad (39)$$

which implies

$$h = \alpha x - \frac{\Omega}{\alpha G}\log x + o(\log x). \quad (40)$$

Substituting eq. (40) into eq. (37), we find

$$h' = \alpha - \frac{\Omega}{\alpha G}x^{-1} - \frac{\Omega^2}{\alpha^3 G^2}x^{-2}\log x + o(x^{-2}\log x), \quad (41)$$

which implies

$$h = \alpha x - \frac{\Omega}{\alpha G}\log x + \frac{\Omega^2}{\alpha^3 G^2}x^{-1}\log x + o(x^{-1}\log x). \quad (42)$$

In principle, any constant of integration can be added to this expression, and this reflects the fact that there is translational invariance in the problem, *i.e.*, if $h(x)$ is a solution of eq. (8), then a profile obtained by shifting $h(x)$ along the x-axis is also a solution of this equation. Without loss of generality, we choose the constant of integration to be zero, which breaks this translational invariance and allows selecting a unique solution from the infinite set of solutions.

Substituting eq. (42) into eq. (37), we find

$$\begin{aligned} h' = &\alpha - \frac{\Omega}{\alpha G}x^{-1} - \frac{\Omega^2}{\alpha^3 G^2}x^{-2}\log x \\ &-\frac{U}{\alpha^2 G}x^{-2} - \frac{\Omega^3}{\alpha^5 G^3}x^{-3}\log^2 x \\ &+\frac{\Omega^3}{\alpha^5 G^3}x^{-3}\log x + o(x^{-3}\log x), \end{aligned} \quad (43)$$

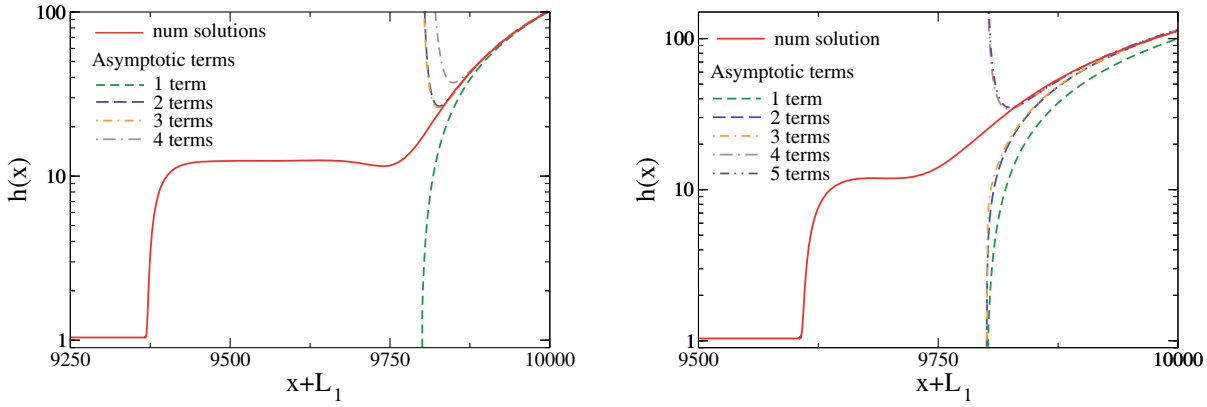

Fig. 2. Left panel: Comparison between a numerical solution for $\Omega = 0$ when $\alpha = 0.5$ and $U = 0.084$ and the expansion for $h(x)$ given by eq. (46) with 1-4 terms. Right panel: Comparison between a numerical solution for $\Omega = 0.001$ when $\alpha = 0.5$ at $U = 0.076$ and the expansion for $h(x)$ given by eq. (44) with 1-5 terms. $L_1 = 9800$, $L_2 = 200$.

which implies

$$h = \alpha x - \frac{\Omega}{\alpha G}\log x + \frac{\Omega^2}{\alpha^3 G^2}x^{-1}\log x \tag{44}$$
$$+\left(\frac{\Omega^2}{\alpha^3 G^2} + \frac{U}{\alpha^2 G}\right)x^{-1}$$
$$-\frac{\Omega^3}{2\alpha^5 G^3}x^{-2}\log^2 x + o(x^{-2}\log x). \tag{45}$$

The procedure described above can be continued to obtain more terms in the asymptotic expansion of h as $x \to \infty$. Note that all the terms in this expansion, except the first two, will be of the form $x^{-m}\log^n x$, where m is a positive integer and n is a non-negative integer. It should also be noted that the presence of the logarithmic terms in the asymptotic expansion of h is wholly due to the quadratic contribution to the flux in eq. (7) that here results from a lateral temperature gradient. Without this term, *i.e.*, for $\Omega = 0$, the expansion (37) for h' does not contain the term proportional to h^{-1}. This implies that after substituting $h(x) = \alpha x + o(x)$ in this expansion, no term proportional to x^{-1} will appear, and, therefore, integration will not lead to the appearance of a logarithmic term. In fact, it is straightforward to see that for $\Omega = 0$ an appropriate ansatz for h is

$$h \sim \alpha x + D_1 x^{-1} + D_2 x^{-2} + D_3 x^{-3} + \cdots, \tag{46}$$

implying that

$$D_1 = \frac{U}{\alpha^2 G}, \qquad D_2 = -\frac{C_0}{2\alpha^3 G},$$
$$D_3 = -\frac{1}{3}\left(\frac{2U^2}{\alpha^5 G} + \frac{3}{\alpha^3 G} - \frac{6U}{\alpha^2 G^2}\right), \quad \ldots. \tag{47}$$

Note that the presence of a logarithmic term in the asymptotic behaviour of h was also observed by Münch and Evans [16] in a related problem of a liquid film driven out of a meniscus by a thermally induced Marangoni shear stress onto a nearly horizontal fixed plane. They find the following asymptotic behaviour of the solution, given with our definition of the coordinate system

$$h(x) \sim h_0(x) + D_0 + D_1 \exp(-D^{1/2}x) \quad \text{as} \quad x \to \infty, \tag{48}$$

where $h_0 = x/D - \log x + o(1)$, D is the parameter measuring the relative importance of the normal component of gravity and D_0 and D_1 are arbitrary constants. The constant D_0 reflects the fact that there is translational invariance in the problem and it can be set to zero without loss of generality. An analysis performed along the lines indicated above shows that a more complete expansion has the form

$$h(x) \sim \frac{x}{D} - \log x + D\,x^{-1}\log x + Dx^{-1}$$
$$+\frac{D^2}{2}x^{-2}\log^2 x + \cdots. \tag{49}$$

Note that there is no need to include the exponentially small term as it is asymptotically smaller than all the other terms of the expansion.

4 Numerical results

In this section, we present numerical solutions of eq. (8). We solve the equation on the domain $[-L_1, L_2]$. At $x = -L_1$, we impose the boundary conditions $h'(-L_1) = 0$ and $h''(-L_1) = 0$. At $x = L_2$, we impose the boundary condition obtained by truncating the asymptotic expansion (44) for $\Omega \neq 0$ or (46) for $\Omega = 0$ and evaluating it at $x = L_2$. We additionally impose a condition for the derivative of h at L_2 obtained by differentiating the asymptotic expansion for h and evaluating it at $x = L_2$. To solve this boundary-value problem numerically, we use the continuation and bifurcation software AUTO-07p (see refs. [39, 40]). A description of the application of numerical continuation techniques to thin film problems can be found in sect. 4b of the review in ref. [41], in sect. 2.10 of ref. [30], and in refs. [42–44]. We perform our numerical calculations on a domain with $L_1 = 9800$ and $L_2 = 200$ and choose $G = 0.001$.

In fig. 2, we compare the numerical solutions with the derived asymptotic expressions for h as $x \to \infty$, when the inclination angle is $\alpha = 0.5$. In the left panel, $\Omega = 0$ and $U = 0.084$. The solid line shows a numerically computed profile, in which we can identify three regions, namely, a thin precursor film, a foot, and a bath region. We also show the truncated asymptotic expansion (46) with one, two, three and four terms included, as is indicated in the legend. In the right panel, $\Omega = 0.001$ and $U = 0.076$. The solid line shows a numerically computed profile, the remaining lines correspond to the truncated asymptotic expansion (44) with one, two, three, four and five terms included, as is indicated in the legend. In both cases, we can observe that the numerically computed profiles agree with the derived asymptotic expansions and including more terms gives better agreement.

In fig. 3, we present bifurcation diagrams showing the dependence of a certain solution measure quantifying the foot length on the velocity of the plate for $\Omega = 0$. More precisely, the measure is defined by $l_f = (V - V_0)/(h_f - h_p)$, where $V = \int_{-L_1}^{L_2}(h(x) - h_p)\mathrm{d}x$, h_f is the characteristic foot height, h_p is the precursor film height for the corresponding velocity, and V_0 is equal to V computed at $U = 0$.

We observe that there is a critical inclination angle, $\alpha_c \approx 0.1025$, such that for $\alpha < \alpha_c$, the bifurcation curve increases monotonically towards a vertical asymptote at some value of the velocity, which we denote by U_∞. This can be observed in the left panels of fig. 3 when $\alpha = 0.1$. When $\alpha > \alpha_c$, we observe a snaking behaviour where the bifurcation curve oscillates around a vertical asymptote at $U = U_\infty$ with decaying amplitude of oscillations. This can be observed in the right panels of fig. 3 when $\alpha = 0.5$. We note that in this case there is an infinite but countable number of saddle-nodes at which the slope of the bifurcation curve is vertical.

Note that U_∞ is different for each inclination angle. The character of the steady solutions is discussed below in fig. 6.

We note that in the case with an additional temperature gradient ($\Omega \neq 0$) we observe qualitatively similar bifurcation diagrams. If an inclination angle is below a critical value (which now depends on Ω), then the bifurcation diagrams are monotonic. Otherwise, the bifurcation diagrams show snaking behaviour, as for the case of zero temperature gradient. An example of snaking bifurcation curves for $\alpha = 0.5$ and $\Omega = -0.001$, 0 and 0.001 is given in fig. 4, and the corresponding bifurcation curves are shown by dashed, solid and dot-dashed lines. We can observe that as the temperature-gradient parameter Ω is increased/decreased, the vertical asymptote is shifted to the left/right. We can also conclude that if the temperature gradient pulls the liquid downwards, steady-state solutions of this bifurcation branch exist for larger values of U. Otherwise, if the temperature gradient pulls the liquid upwards, steady-state solutions of this bifurcation branch exist for smaller values of U. The right panel of fig. 4 shows three profiles for $l_f = 300$ by dashed, solid and dot-dashed lines for $\Omega = 0.001$, 0 and -0.001, respectively. We observe that the foot height decreases as Ω decreases.

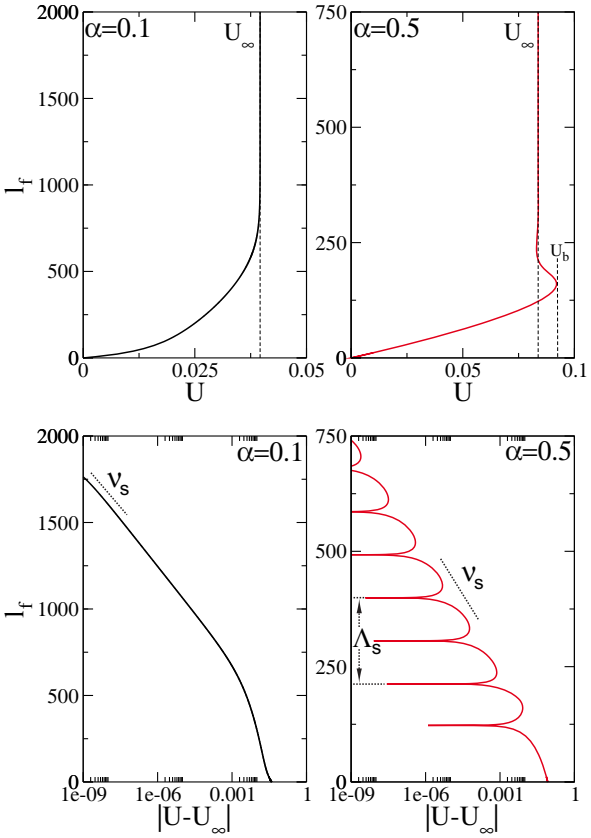

Fig. 3. Comparison of bifurcation diagrams for two inclination angles as stated in the panels in the case without temperature gradient ($\Omega = 0$). Top: Left panel: Asymptotic monotonic increase of the foot length l_f towards the vertical asymptote at $U = U_\infty$ as a function of the plate velocity U for $\alpha = 0.1$, which is below α_c. Right panel: Snaking behaviour of the foot length l_f where the bifurcation curve oscillates around a vertical asymptote at $U = U_\infty$ with decaying amplitude of oscillations as a function of the plate velocity U for $\alpha = 0.5$, which is above α_c. Note the appearance of pairs of saddle nodes (the first being at U_b) where the system successively switches branches and "snakes" around U_∞. Bottom: In order to illustrate the different behaviour for angles below and above α_c, we show the foot-length measure l_f *versus* $|U - U_\infty|$ in a semi-log plot. Left panel: The semi-log plot shows an asymptotic monotonic growth in U. Right panel: An exponential–oscillating periodic decay is clearly shown. A periodic structure with a snaking wavelength Λ_s and an exponential decay rate ν_s appears after U_b (bifurcation: appearance of the first saddle node).

In order to illustrate the different behaviour for angles below and above α_c, we also show the foot length measure, l_f, *versus* $|U - U_\infty|$ in a semi-log plot, see the lower left and right panels of fig. 3 for $\alpha = 0.1$ and $\alpha = 0.5$, respectively. For $\alpha = 0.1$, it can be clearly seen that the bifurcation curve approaches the vertical asymptote exponentially with a rate which we denote by

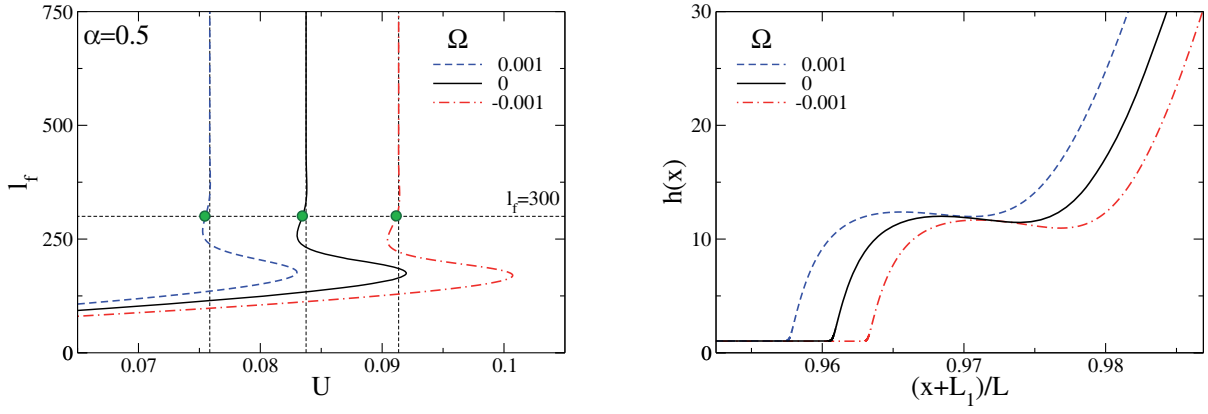

Fig. 4. Left panel compares bifurcation diagrams for different temperature gradients Ω as shown in the legend for an inclination angle $\alpha = 0.5$. The green filled circles indicate the points at which $l_f = 300$ and the corresponding film profiles are shown in the right panel. Note that the snaking behaviour is present. The temperature gradient Ω shifts the vertical asymptote at U_∞ and changes the characteristic foot height at U_∞.

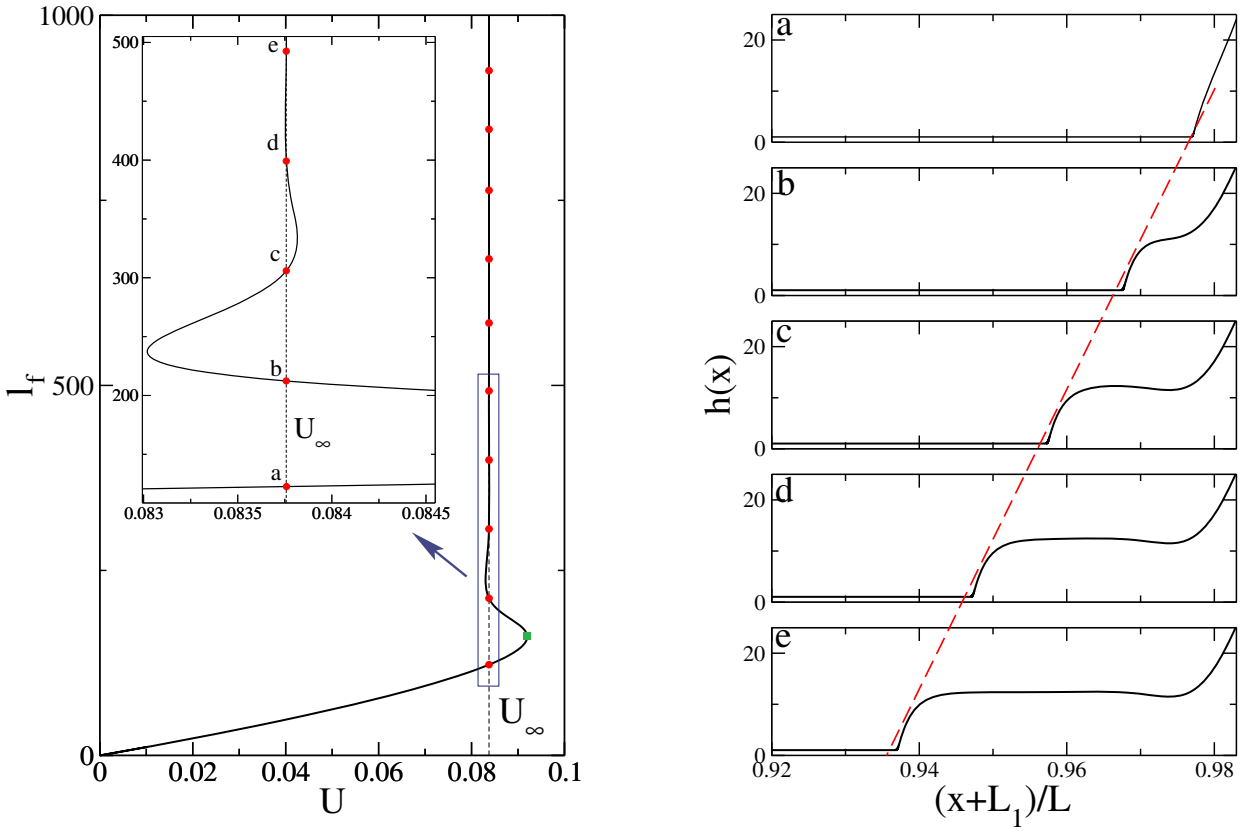

Fig. 5. Film profiles at plate velocity U_∞ for $\alpha = 0.5$. Left panel: Bifurcation diagram. The red filled circles correspond to film solutions at plate velocity U_∞. The inset shows a blow-up of the region with the first five solutions. Note the appearance of a characteristic snaking behaviour around U_∞. The letters in the inset correspond to the film profiles depicted in the right panel. Note the appearance of undulations on top of the foot-like part of the solution as the foot becomes longer. The numerical domain size used is $L = 10000$, $L_1 = 9800$. Note that the first profile (a) corresponds to a meniscus solution. It is located on the lowest branch before the bifurcation curve folds back at U_b (the green square). The red dashed line indicates a linear increase in foot length.

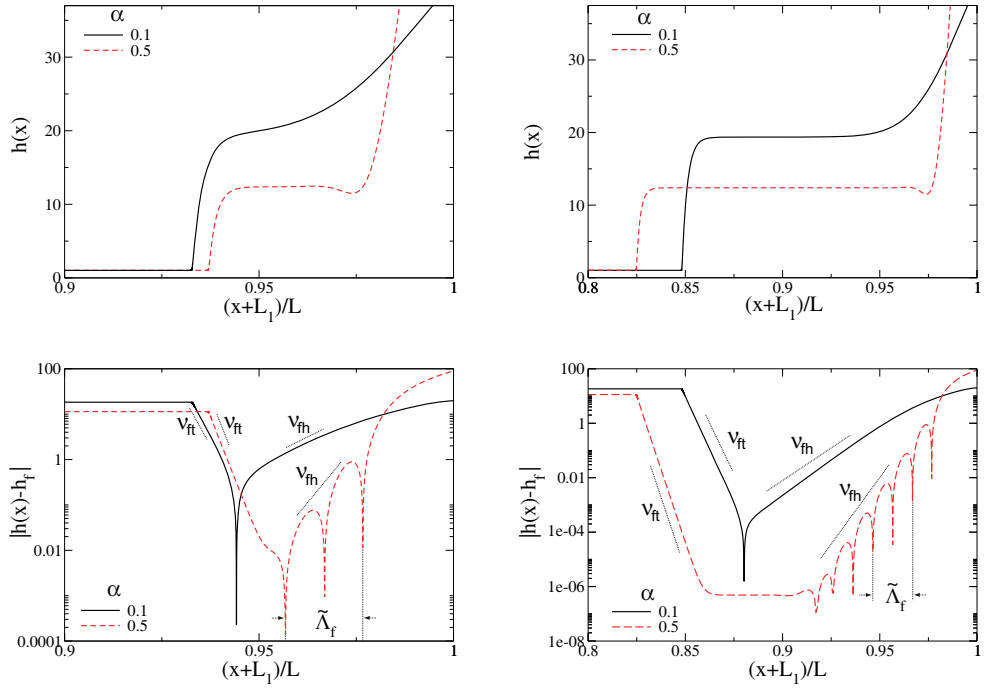

Fig. 6. Film profiles below and above α_c given as solid and dashed lines, respectively. Left panel: Shown are film profiles for $\alpha = 0.1$ close to U_∞ and for $\alpha = 0.5$ at U_∞. Right panel: In order to show the appearance of undulations on top of the foot above α_c, we represent in bottom panels $|h(x) - h_f|$ *versus* $(x + L_1)/L$ in a semi-log plot, where $L_1 = 9800$, $L = 10000$ is the numerical domain size and h_f is the characteristic foot height calculated for each inclination angle α by solving eq. (8) for $h' = 0$, $h'' = 0$ and $h''' = 0$ (using the numerically obtained value of the flux C_0). Observe the exponential approach with rate $\nu_{\rm fh}$ of the foot height from the bath side, and as well the exponential departure with rate $\nu_{\rm ft}$ from the foot height towards the precursor film (see main text for details). Note that the measured foot wavelength is $\Lambda_f = \tilde{\Lambda}_f L$.

ν_s. For $\alpha = 0.5$, we can see that the approach of the vertical asymptote is exponential with the snaking wavelength tending to a constant value, which we denote by Λ_s.

Figure 5 shows the identified snaking behaviour for $\alpha = 0.5$ in more detail. In the left panel, we see the bifurcation diagram where the red filled circles correspond to solutions at U_∞. In the chosen solution measure, the solutions appear equidistantly distributed. In the inset, the first five solutions are indicated and labeled by (a)-(e) and the corresponding film profiles are shown in the right panel. The dashed line in the right panel confirms the linear growth of the foot length.

The differences in film profiles for angles below and above α_c can be seen in fig. 6 that shows solutions for velocities close to U_∞ for $\alpha = 0.1$ and at U_∞ for 0.5 by solid and dashed lines, respectively. In the left and the right panels, we compare short-foot and long-foot solutions, respectively, with similar foot lengths. To emphasise the differences, we represent the profiles in a semi-log plot $|h(x) - h_f|$ *versus* $(x + L_1)/L$ in the bottom panels. For $\alpha = 0.1$ we see no undulations —only exponential decays at a rate denoted by $\nu_{\rm fh}$ from the bath to the foot and at a rate denoted by $\nu_{\rm ft}$ from the foot to the precursor. However, for $\alpha = 0.5$ we observe an oscillatory exponentially decaying behaviour at a rate denoted by $\nu_{\rm fh}$ with a wavelength denoted by Λ_f in the region between the bath and the foot. In the region between the foot and the precursor film, we again observe an exponential decay.

Figures 3 to 5 allow us to recognise the observed behaviour as collapsed heteroclinic snaking (see footnote [1]): The bifurcation curve in fig. 5 is a snaking curve of heteroclinic orbits, *i.e.*, each point on the curve represents a heteroclinic orbit connecting the fixed points for precursor film $\boldsymbol{y}_p$ and bath surface $\boldsymbol{y}_b$ of the dynamical system (9)-(11), namely, if h_p and h_f are the heights of the precursor film and the foot and α is the inclination angle, then the fixed points are $\boldsymbol{y}_p = (1/h_p, 0, 0)$ and $\boldsymbol{y}_b = (0, \alpha, 0)$, respectively. In the limit $U \to U_\infty$ the curve approaches a heteroclinc chain consisting of two heteroclinc orbits — one connecting the fixed points precursor film $\boldsymbol{y}_p$ and foot $\boldsymbol{y}_f = (1/h_f, 0, 0)$ and the other one connecting foot $\boldsymbol{y}_f$ and bath $\boldsymbol{y}_b$. Figure 5 (left) shows the first 5 heteroclinic orbits connecting $\boldsymbol{y}_p$ and $\boldsymbol{y}_b$ — all at $U = U_\infty$. In sect. 5 it is proved that at $U = U_\infty$ there exists a countable infinite number of such heteroclinic connections.

The values of h_p and h_f at $U = U_\infty$ are shown in fig. 7 as functions of α by dashed and solid lines, respectively. In fig. 8, we show the dependence of the eigenvalues of the Jacobians of system (9)-(11) at fixed points $\boldsymbol{y}_p$ and $\boldsymbol{y}_f$ at $U = U_\infty$ as functions of α (also cf. beginning of sect. 5). We note that for the precursor film all the eigenvalues are real, two of them are positive and one is negative independently of the angle. We denote these eigenvalues by $\lambda_{p,i}$,

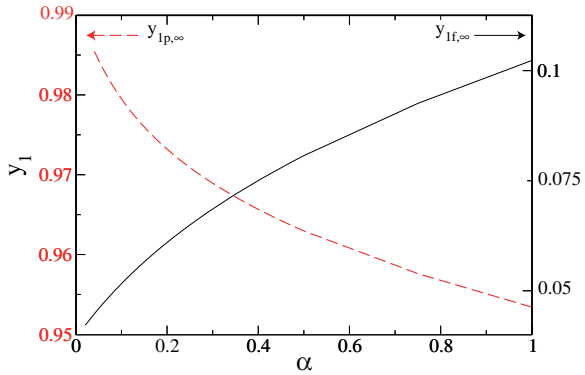

Fig. 7. y_1 ($y_1 = 1/h$) at fixed points for precursor film height, h_p, ($y_{1p} = 1/h_p$), and foot film height, h_f, ($y_{1f} = 1/h_f$), *versus* inclination angle α at U_∞ shown by dashed and solid lines, respectively, in a double entry plot. Note that the correct numerically obtained flux C_0 is needed at each α to determine the fixed points. The left side of the ordinate axis corresponds to the precursor film, the right side corresponds to the foot.

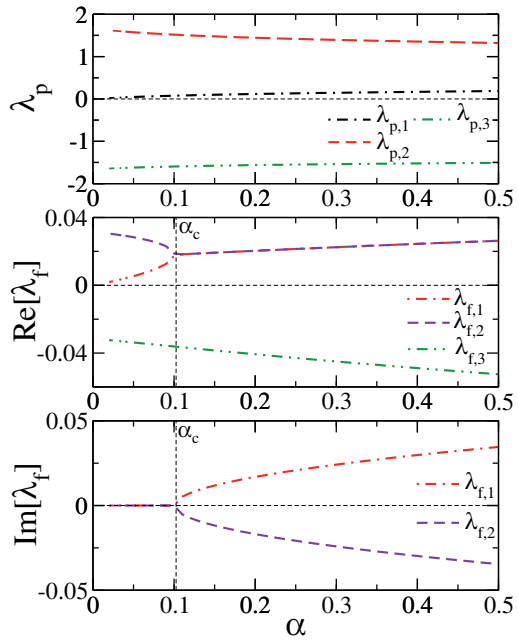

Fig. 8. Eigenvalues at corresponding U_∞ for each α. Upper panel: Shown are the three eigenvalues λ_p *versus* α for the fixed point corresponding to the precursor film. Note that all the eigenvalues are real. Middle and bottom panels: Shown are the real and the imaginary parts, respectively, of the three eigenvalues λ_f *versus* α for the fixed corresponding to the foot.

$i = 1, 2, 3$. However for the foot, the behaviour of the eigenvalues changes for angles below and above a critical value and it turns out that this critical angle is the same as the critical angle at which monotonic bifurcation diagrams change to snaking, *i.e.*, $\alpha_c \approx 0.1025$. We observe that for $\alpha < \alpha_c$ all the eigenvalues for the foot are real —two are positive and denoted by $\lambda_{f,1}$ and $\lambda_{f,2}$ so that $\lambda_{f,1} < \lambda_{f,2}$ and one is negative and is denoted by $\lambda_{f,3}$. However, for $\alpha > \alpha_c$ there is a negative real eigenvalue, $\lambda_{f,3}$, and a pair of complex conjugate eigenvalues with positive real parts, $\lambda_{f,1}$ and $\lambda_{f,2}$. Table 2 shows the values of eigenvalues $\lambda_{f,i}$, $i = 1, 2, 3$, for $\alpha = 0.1$ and 0.5.

Table 2. Eigenvalues at fixed point $\boldsymbol{y}_f = (y_{1f}, 0, 0)$ with $y_{1f} = 1/h_f$ for $\alpha = 0.1$ close to U_∞ and for $\alpha = 0.5$ at U_∞. Note that all the eigenvalues are real for $\alpha = 0.1$, whereas for $\alpha = 0.5$ one eigenvalue is real and negative and two are complex conjugates with positive real parts. See fig. 8.

$\boldsymbol{\alpha}$	h_f	y_{1f}	$\lambda_{f,1}$	$\lambda_{f,2}$	$\lambda_{f,3}$
0.1	19.3732	0.0516	0.0173	0.0188	−0.0361
0.5	12.3922	0.0807	0.0263 +i 0.0346	0.0263 −i 0.0346	−0.0525

Table 3. Shown is the comparison of the exponential decays $\nu_{\rm ft}$, $\nu_{\rm fh}$ with the eigenvalue ν from the linear stability analysis for $\alpha = 0.1$ close to U_∞ and for $\alpha = 0.5$ at U_∞ for solutions with a short foot. See fig. 6.

$\boldsymbol{\alpha}$	$\nu = \mathrm{Re}[\lambda_{f,3}]$	$\nu_{\rm ft}$	$\nu = \mathrm{Re}[\lambda_{f,1}]$	$\nu_{\rm fh}$
0.1	−0.0361	−0.0403	0.0173	0.0152
0.5	−0.0525	−0.0497	0.0263	0.0278

Table 4. Shown is the comparison of the exponential decays $\nu_{\rm ft}$, $\nu_{\rm fh}$ with the eigenvalue ν from the linear stability analysis for $\alpha = 0.1$ close to U_∞ and for $\alpha = 0.5$ at U_∞ for solutions with a long foot. See fig. 6.

$\boldsymbol{\alpha}$	$\nu = \mathrm{Re}[\lambda_{f,3}]$	$\nu_{\rm ft}$	$\nu = \mathrm{Re}[\lambda_{f,1}]$	$\nu_{\rm fh}$
0.1	−0.0361	−0.0356	0.0173	0.0155
0.5	−0.0525	−0.0463	0.0263	0.0255

Table 5. Shown is the comparison of the wavelength of snaking Λ_s from the bifurcation diagram and wavelength of the undulations of the foot Λ_f from the foot-like profile with the wavelength Λ calculated from the eigenvalues $\lambda_{f,i}$ at U_∞ for $\alpha = 0.5$. Note the locking between $\Lambda \approx \Lambda_s \approx \Lambda_f$. See fig. 3 and fig. 6.

$\boldsymbol{\alpha}$	Λ=2π/Im[$\lambda_{f,1}$]	Λ_f (long)	Λ_f (short)	Λ_s
0.5	181.6987	202.6920	198.8801	184.7657

In tables 3 and 4, we compare $\mathrm{Re}[\lambda_{f,3}]$ with the exponential rate $\nu_{\rm ft}$ characterising the connection between the foot and the precursor film, and $\mathrm{Re}[\lambda_{f,1}]$ with the exponential rate $\nu_{\rm fh}$ characterising the connection between the foot and the bath. Table 3 corresponds to a short foot, while table 4 corresponds to a long foot. For $\alpha = 0.5$ the plate velocity is equal to U_∞, while for $\alpha = 0.1$ we choose a foot of approximately the same lengths as for $\alpha = 0.5$ and we note that for $\alpha = 0.1$ the bifurcation curves do not reach U_∞, but for the chosen foot the velocities coincide with U_∞ up to at least seven significant digits. The results show that there is good agreement between $\mathrm{Re}[\lambda_{f,3}]$ and $\nu_{\rm ft}$ and between $\mathrm{Re}[\lambda_{f,1}]$ and $\nu_{\rm fh}$ for both values of α and for both foot lengths, with a maximal error below 12%.

Table 6. Shown is the comparison of the exponential decay constant $1/\nu_S$ from the bifurcation diagrams with the eigenvalues $\lambda_{f,i}$ calculated from the linear stability analysis for $\alpha = 0.1$ and $\alpha = 0.5$. See fig. 3.

$\boldsymbol{\alpha}$	$\mathrm{Re}[\lambda_{f,1}]$	$1/\nu_s$
0.1	0.0173	0.0151
0.5	0.0263	0.0284

In table 5 we compare $\Lambda = 2\pi/\mathrm{Im}[\lambda_{f,1}]$ with the wavelength of the oscillations on the foot, Λ_f, for a long and a short foot, and with the wavelength of oscillations in snaking bifurcation diagrams, Λ_s, when $\alpha = 0.5$. The results show that there is good agreement between Λ and Λ_s —the error is below 2%, and between Λ and Λ_f for both foot lengths —the error is below 12%[2].

In table 6, we compare $\mathrm{Re}[\lambda_{f,1}]$ with the exponential rate $1/\nu_s$, where ν_s is characterises the rate at which the bifurcation diagrams approach the vertical asymptotes. We again observe good agreement for both values of α, with an error below 13%.

The close agreement between the eigenvalues corresponding to the foot and the quantities obtained from the bifurcation diagrams and the foot profiles is explained in the next section.

5 Collapsed heteroclinic snaking

In what follows, our aim is to explain the snaking behaviour observed in our numerical results, see the left panels of fig. 3 and fig. 5. We perform our analysis in the way similar to the Shilnikov-type method for studying subsidiary homoclinic orbits near the primary one explained in, *e.g.*, ref. [22]. For simplicity, we consider the case of zero temperature gradient, *i.e.*, we set $\Omega = 0$. First, let us consider fixed points of system (9)-(11) with $y_1 \neq 0$. For such fixed points, $y_2 = y_3 = 0$ and y_1 satisfies the equation

$$f(y_1) \equiv y_1^3 - \frac{U}{C_0} y_1^2 + \frac{G\alpha}{C_0} = 0. \tag{50}$$

It can be easily checked that this cubic polynomial has a local maximum at $y_1^a = 0$ and a local minimum at a positive point y_1^b. Moreover, $f(y_1^a) > 0$ implying that there is always a fixed point with a negative value of the y_1-coordinate. We disregard this point, since physically it would correspond to negative film thickness. Also, assuming that $G\alpha < (4/27)(U^3/C_0^2)$, we obtain $f(y_1^b) < 0$, which implies that there are two positive roots a_1 and a_2 of the cubic polynomial satisfying $a_1 < a_2$. This implies that there are two more fixed points, $\boldsymbol{y}_f = (a_1, 0, 0)$ and $\boldsymbol{y}_p = (a_2, 0, 0)$. The point $\boldsymbol{y}_f$ corresponds to the foot and the point $\boldsymbol{y}_p$ corresponds to the precursor film.

To analyse stability of these fixed points, we compute the Jacobian at these points,

$$J_{\boldsymbol{y}_{f,p}} = \begin{pmatrix} 0 & -a_{1,2}^2 & 0 \\ 0 & 0 & 1 \\ 2Ua_{1,2} - 3C_0 a_{1,2}^2 & 6a_{1,2}^7 - 3a_{1,2}^4 + G & 0 \end{pmatrix}. \tag{51}$$

A simple calculation shows that for both, $\boldsymbol{y}_f$ and $\boldsymbol{y}_p$, all the eigenvalues have non-zero real parts implying that these points are hyperbolic. Moreover, both points have two-dimensional unstable manifolds and one-dimensional stable manifolds. Our numerical simulations presented in the previous section show that for the values of the inclination angle α that we have considered, there exists a value of the plate speed, U_∞, such that in the vicinity of this value there exist steady solutions for which the foot length can be arbitrarily long, see fig. 3. (In fact, we found that this is true if α is smaller than a certain transition value $\alpha_T \approx 2.42$. For larger values of α, the solution branches originating from $U = 0$ are not anymore characterised by such limiting velocities. In the present manuscript, we do not consider such solutions and assume therefore that $\alpha < \alpha_T$. Other types of solutions will be analysed elsewhere.) We conclude that at $U = U_\infty$, there exists a heteroclinic chain connecting the fixed points $\boldsymbol{y}_p$, $\boldsymbol{y}_f$ and $\boldsymbol{y}_b$. As was discussed in the previous section, in the top panel of fig. 8, we can observe that for point $\boldsymbol{y}_p$ all the eigenvalues are real at $U = U_\infty$ implying that this point is a saddle. The two bottom panels of fig. 8 demonstrate that there is a critical inclination angle $\alpha_c \approx 0.1025$ such that for $\alpha \leq \alpha_c$, all the eigenvalues for $\boldsymbol{y}_f$ are real, whereas for $\alpha > \alpha_c$, one eigenvalue is real and negative and there is a pair of complex conjugate eigenvalues with positive real parts. Therefore, for $\alpha \leq \alpha_c$, point $\boldsymbol{y}_f$ is a saddle, but for $\alpha > \alpha_c$, it is a saddle-focus. In the following Theorem, we analytically prove that if $\boldsymbol{y}_f$ is a saddle-focus, there exists an infinite but countable number of subsidiary heteroclinic orbits connecting $\boldsymbol{y}_p$ and $\boldsymbol{y}_b$ that lie in a sufficiently small neighbourhood of the heteroclinic chain connecting $\boldsymbol{y}_p$, $\boldsymbol{y}_f$ and $\boldsymbol{y}_b$. This explains the existence of an infinite but countable number of steady-state

[2] The wavelength Λ_f is measured using the $|h(x) - h_f|$ data that are presented in fig. 6. The distances between divergencies at x_i, *i.e.*, at the positions where $|h(x_i) - h_f| \to 0$ correspond to a semi-period of the foot wavelength Λ_f. The value of Λ_f is determined as the average of *all* available $(x_{i+1} - x_i)$. Note that we can observe only up to five semi-periods due to the exponentially decreasing amplitude of the modulation and the restricted number of digits of the profile data obtained from AUTO-07p. As a result, the undulations are not detectable when their amplitude decreases below $\approx 10^{-7}$. The effect is clearly seen in the lower left panel of fig. 6, where for $\alpha = 0.5$ we observe a plateau between the visible undulations and the exponential decay with rate ν_{ft} towards the precursor film. Further, there is a limited accuracy due to the number of discretisation points in space. The measurement of Λ_s is more exact as it makes use of the data employed in the $|U - U_\infty|$ graph (figs. 3 and 6). In contrast to the thickness profile data, these bifurcation curve data are of a high precision allowing us to see about 10 semi-periods. Λ_s is measured only taking values of the semi-periods that have already converged to 3 significant digits, *i.e.*, at $|U - U_\infty| \to 0$ (cf. fig. 3). Several such $l_f(i+1) - l_f(i)$ values corresponding to the length of a semi-period of the snaking wavelength are then averaged to obtain Λ_s. This ensures that nonlinear effects do not enter the picture (that are likely to be present in the Λ_f measurement).

solutions having different foot lengths observed in the previous section, see the left panels of fig. 3 and fig. 5. Note that an infinite but countable number of solutions has also been observed in, *e.g.*, ref. [16] for the case of a liquid film rising onto a resting inclined plate driven by Marangoni forces due to a temperature gradient. There, the authors identify type 1 and type 2 solutions with small and large far-field thicknesses, respectively. These correspond to our precursor and foot height, respectively. It is observed that for certain parameter values there exists an infinite but countable number of type 2 solutions. Similar to our case, this can be explained by the existence of a heteroclinic chain connecting the three fixed points. However, unlike here, in ref. [16] the chain connects the fixed point for the thick film along its unstable manifold with the fixed point for the thin film thickness that is then connected with the fixed point for the bath.

Theorem. Consider a three-dimensional system

$$\boldsymbol{y}' = \boldsymbol{f}(\boldsymbol{y}, \beta), \qquad \boldsymbol{y} \in \mathbb{R}^3, \tag{52}$$

where β denotes a parameter (that takes the role of the plate velocity U above). We assume that there exist three fixed points, which we denote by $\boldsymbol{y}_p$, $\boldsymbol{y}_f$ and $\boldsymbol{y}_b$, when β is sufficiently close to a number β_0 (*i.e.*, a number like the plate velocity U_∞). We additionally assume that $\boldsymbol{y}_p$ and $\boldsymbol{y}_b$ have a two-dimensional unstable manifold $W_u(\boldsymbol{y}_p)$ and a two-dimensional stable manifold $W_s(\boldsymbol{y}_b)$, respectively, and that $\boldsymbol{y}_f$ is a saddle-focus fixed point with a one-dimensional stable manifold $W_s(\boldsymbol{y}_f)$ and a two-dimensional unstable manifold $W_u(\boldsymbol{y}_f)$ (*i.e.*, the eigenvalues of the Jacobian at $\boldsymbol{y}_f$ are $-\lambda_1$, $\lambda_2 \pm \mathrm{i}\,\omega$, where $\lambda_1 = \lambda_1(\beta)$, $\lambda_2 = \lambda_2(\beta)$ and $\omega = \omega(\beta)$ are positive real numbers when β is sufficiently close to β_0)[3]. Let us also assume that for $\beta = \beta_0$, there is a heteroclinic orbit $\Gamma_1 \in W_u(\boldsymbol{y}_p) \cap W_s(\boldsymbol{y}_f)$ connecting $\boldsymbol{y}_p$ and $\boldsymbol{y}_f$ and that the manifolds $W_u(\boldsymbol{y}_f)$ and $W_s(\boldsymbol{y}_b)$ intersect transversely so that there is a heteroclinic orbit $\Gamma_2 \in W_u(\boldsymbol{y}_f) \cap W_s(\boldsymbol{y}_b)$ connecting $\boldsymbol{y}_f$ and $\boldsymbol{y}_b$. Then for $\beta = \beta_0$ there is an infinite but countable number of heteroclinic orbits connecting $\boldsymbol{y}_p$ and $\boldsymbol{y}_b$ and passing near $\boldsymbol{y}_f$. Moreover, the difference in "transition times" from $\boldsymbol{y}_p$ to $\boldsymbol{y}_b$ tends asymptotically to π/ω (the meaning of a "transition time" from $\boldsymbol{y}_p$ to $\boldsymbol{y}_b$ will be explained below).

Proof: After a suitable change of variables, the dynamical system $\boldsymbol{y}' = \boldsymbol{f}(\boldsymbol{y}, \beta)$ can be written in the form

$$y_1' = \lambda_2 y_1 - \omega y_2 + \tilde{f}_1(\boldsymbol{y}, \beta), \tag{53}$$

$$y_2' = \omega y_1 + \lambda_2 y_2 + \tilde{f}_2(\boldsymbol{y}, \beta), \tag{54}$$

$$y_3' = -\lambda_1 y_3 + \tilde{f}_3(\boldsymbol{y}, \beta), \tag{55}$$

where $\tilde{f}_i$, $i = 1, 2, 3$, are such that $\partial \tilde{f}_i / \partial y_j = 0$, $i, j = 1, 2, 3$, at $\boldsymbol{y} = \boldsymbol{y}_f$. After such a change of variables, the origin is a stationary point corresponding to $\boldsymbol{y}_f$ and sufficiently close to the origin, the terms $\tilde{f}_1(\boldsymbol{y}, \beta)$, $\tilde{f}_2(\boldsymbol{y}, \beta)$ and $\tilde{f}_3(\boldsymbol{y}, \beta)$ are negligibly small, so that near the origin the dynamical system can be approximated by the linearised system

$$y_1' = \lambda_2 y_1 - \omega y_2, \tag{56}$$

$$y_2' = \omega y_1 + \lambda_2 y_2, \tag{57}$$

$$y_3' = -\lambda_1 y_3. \tag{58}$$

Let Σ_1 be a plane normal to the stable manifold of $\boldsymbol{y}_f$, Γ_1, and located at a small distance ε_1 from $\boldsymbol{y}_f$, *i.e.*, locally Σ_1 is given by

$$\Sigma_1 = \{(y_1, y_2, \varepsilon_1) : y_1, y_2 \in \mathbb{R}\}. \tag{59}$$

Let Σ_2 be part of a plane transversal to the unstable manifold of $\boldsymbol{y}_f$, Γ_2, at some point near $\boldsymbol{y}_f$ and passing through $\boldsymbol{y}_f$ that is locally given by

$$\Sigma_2 = \{(y_1, 0, y_3) : |y_1 - r^*| \le \varepsilon_2, |y_3| \le \varepsilon_3\}. \tag{60}$$

Here $(r^*, 0, 0) \in \Gamma_1$ is sufficiently close to the origin and $\varepsilon_3 < \varepsilon_1$. We denote the upper half-plane of Σ_2, when $y_3 > 0$, by Σ_2^+, *i.e.*, $\Sigma_2^+ = \{\boldsymbol{y} \in \Sigma_2 : y_3 > 0\}$ and let $\Sigma_2^- = \Sigma_2 \backslash \Sigma_2^+$. We choose ε_2 to be sufficiently small so that each trajectory crosses Σ_2 only once. It can be shown that this condition is satisfied when $\varepsilon_2 < \tanh(\lambda_2 \pi/\omega)\, r^*$.

Using cylindrical polar coordinates (r, θ, z), such that $y_1 = r\cos\theta$, $y_2 = r\sin\theta$ and $y_3 = z$, the linearised dynamical system near the origin is given by

$$r' = \lambda_2 r, \tag{61}$$

$$\theta' = \omega, \tag{62}$$

$$z' = -\lambda_1 z. \tag{63}$$

The solution is given by

$$r = r_0 \mathrm{e}^{\lambda_2 x}, \tag{64}$$

$$\theta = \theta_0 + \omega x, \tag{65}$$

$$z = z_0 \mathrm{e}^{-\lambda_1 x}. \tag{66}$$

In the cylindrical polar coordinates, Σ_1 is given by $z = \varepsilon_1$ and Σ_2 is given by

$$\Sigma_2 = \{(r, 0, z) : |r - r^*| \le \varepsilon_2, |z| \le \varepsilon_3\}. \tag{67}$$

Let φ_x be the flow map for the linearised dynamical system. Also, let S be the set in Σ_1 given by

$$S = \{\boldsymbol{y} \in \Sigma_1 : \exists\, x \text{ such that } \varphi_x(\boldsymbol{y}) \in \Sigma_2\}. \tag{68}$$

Then we can define the map

$$\varphi : S \to \Sigma_2 : \boldsymbol{y} \mapsto \varphi_x(\boldsymbol{y}) \text{ for some } x > 0. \tag{69}$$

It can easily be checked that the image of φ is in fact Σ_2^+. Also, it can be easily seen that the set S is the so-called

[3] Here, the unstable manifold of $\boldsymbol{y}_p$ refers to the set of points $\boldsymbol{y}_0$ such that $\phi_t(\boldsymbol{y}_0) \to \boldsymbol{y}_p$ as $t \to -\infty$, where ϕ_t is the solution (or evolution) operator for the given dynamical system, and the stable manifold of $\boldsymbol{y}_b$ refers to the set of points $\boldsymbol{y}_0$ such that $\phi_t(\boldsymbol{y}_0) \to \boldsymbol{y}_b$ as $t \to \infty$. These definitions are consistent with those given, *e.g.*, in ref. [49].

Shilnikov snake, a set bounded by two spirals, s_1 and s_2, given by

$$r = (r^* \pm \varepsilon_2)\mathrm{e}^{-\lambda_2 x}, \quad \theta = -\omega x, \quad z = \varepsilon_1, \tag{70}$$

respectively, where $x \in [(1/\lambda_1)\log(\varepsilon_1/\varepsilon_3), \infty)$, and the following segment of a straight line:

$$r \in \left[(r^* - \varepsilon_2)\left(\frac{\varepsilon_3}{\varepsilon_1}\right)^{\lambda_2/\lambda_1}, (r^* + \varepsilon_2)\left(\frac{\varepsilon_3}{\varepsilon_1}\right)^{\lambda_2/\lambda_1}\right], \tag{71}$$

$$\theta = \frac{\omega}{\lambda_1}\log\left(\frac{\varepsilon_3}{\varepsilon_1}\right), \quad z = \varepsilon_1. \tag{72}$$

Let $l_p = \Sigma_1 \cap W_u(\boldsymbol{y}_p)$ be the intersection of the two-dimensional unstable manifold of $\boldsymbol{y}_p$ and the plane Σ_1, which is locally a straight line given for $\beta = \beta_0$ by the equations $\theta = \theta_p$ and $z = \varepsilon_1$, where θ_p is some constant. As $\theta_p \bmod \pi$ determines the direction of the line, we can choose without out loss of generality,

$$\theta_p \in (-\pi + (\omega/\lambda_1)\log(\varepsilon_3/\varepsilon_1), (\omega/\lambda_1)\log(\varepsilon_3/\varepsilon_1)]. \tag{73}$$

Next, let l_n, $n = 1, 2, \ldots$, be the intersections of the line l_p with set S such that $|l_1| > |l_2| > \cdots$, where $|l_n|$ denotes the length of the segment l_n, $n = 1, 2, \ldots$, see fig. 9. We can see that l_n is given by

$$r \in [(r^* - \varepsilon_2)\exp(-\lambda_2(\pi(n-1) - \theta_p)/\omega), (r^* + \varepsilon_2)\exp(-\lambda_2(\pi(n-1) - \theta_p)/\omega)], \tag{74}$$

$$\theta = \theta_p - \pi(n-1) = \theta_p \bmod \pi, \quad z = \varepsilon_1. \tag{75}$$

Then, we find that $\varphi(l_n)$ is a segment of a line in Σ_2 given by

$$r \in [(r^* - \varepsilon_2), (r^* + \varepsilon_2)], \tag{76}$$

$$\theta = 0, \tag{77}$$

$$z = \varepsilon_1 \exp(-\lambda_1(\pi(n-1) - \theta_p)/\omega). \tag{78}$$

Let $l_b = \Sigma_2 \cap W_s(\boldsymbol{y}_b)$ be the intersection of the two-dimensional stable manifold of $\boldsymbol{y}_b$ and the plane Σ_2. Locally it is a segment of a straight line, and since manifolds $W_u(\boldsymbol{y}_f)$ and $W_u(\boldsymbol{y}_b)$ intersect transversely, this segment of the line is given for $\beta = \beta_0$ by parametric equations

$$r = r^* + as, \quad \theta = 0, \quad z = s, \tag{79}$$

where a is some constant and s is a parameter changing from $-\varepsilon_3$ to ε_3. Note that we can choose ε_3 to be smaller than $\varepsilon_2/|a|$ so that the line l_b intersects all the lines $\varphi(l_n)$, $n = 1, 2, \ldots$, and we denote such intersections points by $\boldsymbol{y}_{b,n}$, $n = 1, 2, \ldots$. Let us denote the preimages of these points with respect to map φ by $\boldsymbol{y}_{p,n}$, $n = 1, 2, \ldots$. Note that $\boldsymbol{y}_{p,n} \in l_n$, $n = 1, 2, \ldots$. Next, since for each $n = 1, 2, \ldots$, point $\boldsymbol{y}_{p,n}$ belongs to the unstable manifold of $\boldsymbol{y}_p$, there is an orbit $\Gamma_{p,n}$ connecting $\boldsymbol{y}_p$ and $\boldsymbol{y}_{p,n}$. Also, by definition of point $\boldsymbol{y}_{p,n}$, it is mapped by the flow map φ_x to point $\boldsymbol{y}_{b,n}$ and the "transition time" from $\boldsymbol{y}_{p,n}$ to $\boldsymbol{y}_{b,n}$ is approximately equal to $x = t_{\mathrm{tr}} = (\pi(n-1) - \theta_p)/\omega$. Note that the difference in "transition times" from $\boldsymbol{y}_{p,n}$ to $\boldsymbol{y}_{b,n}$ and from $\boldsymbol{y}_{p,(n+1)}$ to $\boldsymbol{y}_{b,(n+1)}$ tends to π/ω as n increases. We denote the orbit connecting $\boldsymbol{y}_{p,n}$ with $\boldsymbol{y}_{b,n}$ by $\Gamma_{f,n}$. Finally, since $\boldsymbol{y}_{b,n}$ for each $n = 1, 2, \ldots$, point $\boldsymbol{y}_{p,n}$ belongs to the stable manifold of $\boldsymbol{y}_b$, there is an orbit $\Gamma_{b,n}$ connecting $\boldsymbol{y}_{b,n}$ and $\boldsymbol{y}_b$. We conclude that there is an infinite but countable number of subsidiary heteroclinic orbits connecting points $\boldsymbol{y}_p$ and $\boldsymbol{y}_b$ that are given by $\Gamma_{s,n} = \Gamma_{p,n} \cup \Gamma_{f,n} \cup \Gamma_{b,n}$, $n = 1, 2, \ldots$. Moreover, the difference in "transition times" for two successive orbits $\Gamma_{s,n}$ and $\Gamma_{s,(n+1)}$ taken to get from plane Σ_1 to plane Σ_2 tends to π/ω as $n \to \infty$. Q.E.D.

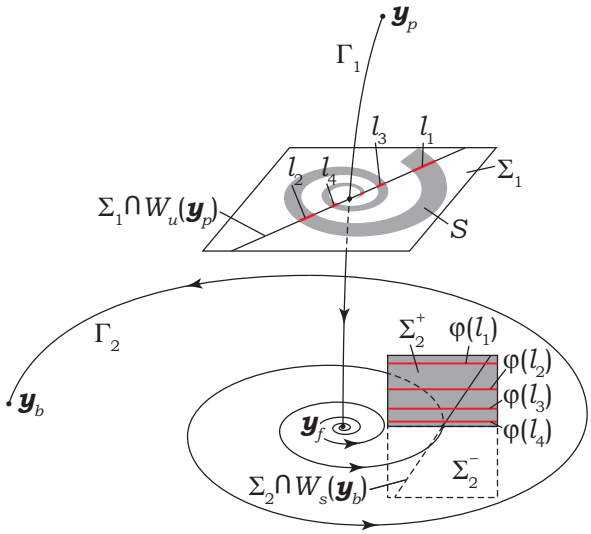

Fig. 9. Schematic representation in the three-dimensional phase-space of the fixed points $\boldsymbol{y}_p$, $\boldsymbol{y}_f$ and $\boldsymbol{y}_b$ of system (52) when $\beta = \beta_0$. The fixed point $\boldsymbol{y}_p$ is a saddle point with two-dimensional unstable manifold, $W_u(\boldsymbol{y}_p)$, and a one-dimensional stable manifold. The fixed point is $\boldsymbol{y}_f$ is a saddle-focus with two-dimensional unstable manifold and a one-dimensional stable manifold. The fixed point $\boldsymbol{y}_b$ is a non-hyperbolic point having two-dimensional stable manifold, $W_s(\boldsymbol{y}_b)$. The fixed points $\boldsymbol{y}_p$ and $\boldsymbol{y}_f$ are connected by the heteroclinic orbit Γ_1 and the fixed points $\boldsymbol{y}_f$ and $\boldsymbol{y}_b$ are connected by the heteroclinic orbit Γ_2.

Remark. Snaking diagrams as those computed in the previous section are obtained by an unfolding of the structurally unstable heteroclinic chain connecting $\boldsymbol{y}_p$, $\boldsymbol{y}_f$ and $\boldsymbol{y}_b$. For β close to β_0 but not necessarily equal to β_0, line $l_p = \Sigma_1 \cap W_u(\boldsymbol{y}_p)$ is locally given by

$$y_2 = b(\beta)y_1 + c(\beta), \quad y_3 = \varepsilon_1, \tag{80}$$

where $c(\beta_0) = 0$ and $b(\beta_0) = \tan(\theta_p)$ (without loss of generality, we can assume that $\theta_p \neq \pi/2 + \pi n$ for any $n \in \mathbb{Z}$). This implies that in a small neighbourhood of point $(0, 0, \varepsilon_1)$, this line can be approximated by

$$y_2 = (b(\beta_0) + \Delta\beta\, b'(\beta_0))y_1 + \Delta\beta\, c'(\beta_0), \quad y_3 = \varepsilon_1, \tag{81}$$

where $\Delta\beta = \beta - \beta_0$. Assuming that $c'(\beta_0) \neq 0$, we obtain that for $\beta \neq \beta_0$ line l_p is shifted in plane Σ_2 and does

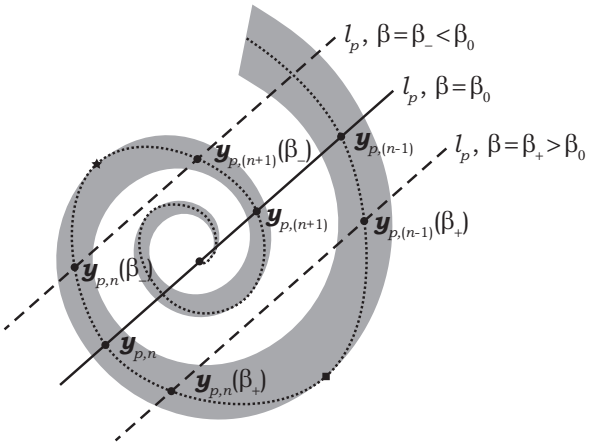

Fig. 10. Schematic representation of the Shilnikov snake, S, in plane Σ_2. The solid line shows line l_p for $\beta = \beta_0$, the dashed lines show lines l_p for $\beta = \beta_+ > \beta_0$ and for $\beta = \beta_- < \beta_0$. The dotted line shows the locus of the points through which heteroclinic orbits connecting $\boldsymbol{y}_p$ and $\boldsymbol{y}_b$ pass for certain values of β near β_0. The black square corresponds to the value of β_+ at which line l_p is tangent to S and at which points $\boldsymbol{y}_{p,(n-1)}$ and $\boldsymbol{y}_{p,n}$ vanish in a saddle-node bifurcation. The star corresponds to the value of β_- at which line l_p is tangent to S and at which points $\boldsymbol{y}_{p,n}$ and $\boldsymbol{y}_{p,(n+1)}$ vanish in a saddle-node bifurcation.

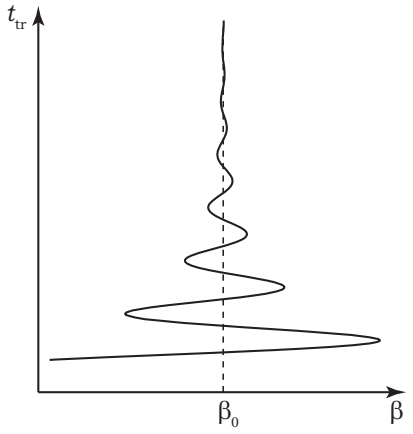

Fig. 11. Bifurcation diagram for heteroclinic orbits connecting $\boldsymbol{y}_p$ and $\boldsymbol{y}_b$.

not pass through point $(0, 0, \varepsilon_1)$, see fig. 10. This implies that for $\beta \neq \beta_0$ line l_p intersects the Shilnikov snake, S, finitely many times. For sufficiently small $\Delta\beta$, we denote by $l_n(\beta)$ the intersection of l_p with S that is obtained by a small shift of l_n for $\beta = \beta_0$. By considerations similar to those in the proof of the previous theorem, it can be shown that in each of the line segments there is a point $\boldsymbol{y}_{p,n}(\beta)$ such that there is a heteroclinic orbit passing through this point and connecting $\boldsymbol{y}_p$ and $\boldsymbol{y}_b$. For $\beta \neq \beta_0$ there is only a finite number of such orbits. Figure 10 schematically shows l_p by a solid line for $\beta = \beta_0$ and by dashed lines for $\beta = \beta_+ > \beta_0$ and $\beta = \beta_- < \beta_0$. In addition, points $\boldsymbol{y}_{p,(n-1)}(\beta_+)$, $\boldsymbol{y}_{p,n}(\beta_+)$, $\boldsymbol{y}_{p,n}(\beta_-)$ and $\boldsymbol{y}_{p,(n+1)}(\beta_-)$ are shown. For certain value of β_+, points $\boldsymbol{y}_{p,(n-1)}(\beta_+)$, $\boldsymbol{y}_{p,n}(\beta_+)$ vanish in a saddle-node bifurcation. This point is indicated by a black square in the figure. At this point, line l_p is tangent to the boundary of S. Also, for certain value of β_-, points $\boldsymbol{y}_{p,n}(\beta_-)$, $\boldsymbol{y}_{p,(n+)}(\beta_-)$ vanish in a saddle-node bifurcation. This point is indicated by a star in the figure. At this point, line l_p is tangent to the boundary of S. The locus of the points through which heteroclinic orbits connecting $\boldsymbol{y}_p$ and $\boldsymbol{y}_b$ pass for certain values of β near β_0 is shown by a dotted line. It can be seen that this line is a spiral, s, that belongs to S, passes through points $\boldsymbol{y}_{p,n}$ and is tangent between transitions from $\boldsymbol{y}_{p,n}$ to $\boldsymbol{y}_{p,(n+1)}$, $n = 1, 2, \ldots$, to the boundary of S given by spiral s_1. It can therefore be concluded that the bifurcation diagram showing the "transition time" for heteroclinic orbits connecting $\boldsymbol{y}_p$ and $\boldsymbol{y}_p$ *versus* parameter β is a snaking curve, shown schematically in fig. 11, similar to the numerically obtained cases in figs. 3, 2 and 5 for $\alpha = 0.5$. There is an infinite number of such orbits in a neighbourhood of β_0 and there is an infinite but countable number of saddle-node bifurcations that correspond to the points at which spiral s touches the boundary of the Shilnikov spiral, S.

We can find that the slope of the line tangent to spiral s_1 is

$$\frac{\mathrm{d}y_2}{\mathrm{d}y_1} = R\tan(\theta + \theta_0), \tag{82}$$

where $R = \sqrt{\lambda_2^2 + \omega^2}$ and $\theta_0 = \tan^{-1}(\omega/\lambda_2)$. Therefore, at the points where line l_p touches spiral s_1, we must have

$$R\tan(\theta_n + \theta_0) = b(\beta_0) + \Delta\beta_n b'(\beta_0), \tag{83}$$

where θ_n and $\Delta\beta_n$ are the values of θ and $\Delta\beta$ corresponding to the n^{th} saddle-node bifurcation. Thus, at these points

$$\theta_n = \tan^{-1}\left(\frac{b(\beta_0)}{R} + \Delta\beta_n\frac{b'(\beta_0)}{R}\right) - \theta_0 - \pi n, \tag{84}$$

for sufficiently large integer n. Equivalently,

$$x_n = -\frac{1}{\omega}\tan^{-1}\left(\frac{b(\beta_0)}{R} + \Delta\beta_n\frac{b'(\beta_0)}{R}\right) + \frac{\theta_0}{\omega} + \frac{\pi}{\omega}n. \tag{85}$$

From this formula, we clearly see that the difference in transition times between two saddle-node bifurcations tends to π/ω. Also, at the saddle-node bifurcations we must have

$$r_n\sin\theta_n = (b(\beta_0) + \Delta\beta_n b'(\beta_0))r_n\cos\theta_n + \Delta\beta_n c'(\beta_0), \tag{86}$$

where $r_n = (r^* + \varepsilon_2)\mathrm{e}^{-\lambda_2 x_n}$, which implies

$$\Delta\beta_n = r_n\frac{\sin\theta_n - b(\beta_0)\cos\theta_n}{c'(\beta_0) + b'(\beta_0)r_n}. \tag{87}$$

From the latter expression, we can conclude that

$$|\Delta\beta_n| = O(r_n) = O(\mathrm{e}^{-\lambda_2 x_n}), \tag{88}$$

which shows that the snaking bifurcation diagram approaches the vertical asymptote at an exponential rate,

and explains the results presented in the bottom right panel of fig. 3 and in table 6.

Also, note that if $\boldsymbol{y}_f$ is a saddle, then the set S is not a spiral but is a wedge-shaped domain. The line l_p then passes through the vertex of this domain for $\beta = \beta_0$ and, generically, intersects it in the neighbourhood of the vertex only for $\beta < \beta_0$ but not for $\beta > \beta_0$ or vice versa. Then, the bifurcation diagram showing the "transition time" for heteroclinic orbits connecting $\boldsymbol{y}_p$ and $\boldsymbol{y}_b$ *versus* parameter β is a monotonic curve instead of a snaking curve shown in fig. 11, similarly to the case in fig. 3 for $\alpha = 0.1$.

In the drawn meniscus problem the difference in transition times between two saddle-node bifurcations (that tends to π/ω) is a measure of the wavelength of the undulations on the foot and is therefore equivalent to the measures Λ_f (as extracted from the steady thickness profiles) and Λ_s (as extracted from the bifurcation curve) discussed in sect. 4 (see, in particular, table 5 where Λ represents π/ω). The overall transition time corresponds to the foot length l_f. Thus one can conclude that the bifurcation diagrams presented in figs. 3 and 5 are explained by the results that have been presented in this section.

6 Conclusions

We have analysed a liquid film that is deposited from a liquid bath onto a flat moving plate that is inclined at a fixed angle to the horizontal and is removed from the bath at a constant speed. We have analysed a two-dimensional situation with a long-wave equation that is valid for small inclination angles of the plate and under the assumption that the longitudinal length scale of variations in the film thickness is much larger than the typical film thickness. The model equation used in most parts of our work includes the terms due to surface tension, the disjoining (or Derjaguin) pressure modelling wettability, the hydrostatic pressure and the lateral driving force due to gravity, and the dragging by the moving plate. To further illustrate a particular finding, we have also considered the situation where an additional lateral Marangoni shear stress results from a linear temperature gradient along the substrate direction. Our main goal has been to analyse selected steady-state film thickness profiles that are related to collapsed heteroclinic snaking.

First, we have used centre manifold theory to properly derive the asymptotic boundary conditions on the side of the bath. In particular, we have obtained asymptotic expansions of solutions in the bath region, when $x \to \infty$. We found that in the absence of the temperature gradient, the asymptotic expansion for the film thickness, h, has the form $h \sim \sum_{n=-1}^{\infty} D_n x^{-n}$, where without loss of generality D_0 can be chosen to be zero (fixing the value of D_0 corresponds to breaking the translational invariance of solutions and allows selecting a unique solution from the infinite family of solutions that are obtained from each other by a shift along the x-axis). In the presence of the temperature gradient, this asymptotic expansion is not valid, but instead consists of terms proportional to x, $\log x$ and $x^{-m} \log^n x$, where m and n is a positive and a non-negative integer, respectively. Note that our systematically obtained sequence differs from the one employed in ref. [16].

Next, we have obtained numerical solutions of the steady-state equation and have analysed the behaviour of selected solutions as the plate velocity and the temperature gradient are changed. When changing the plate velocity, we observe that the bifurcation curves exhibit collapsed heteroclinic snaking when the plate inclination angle is larger than a certain critical value, namely, they oscillate around a certain limiting velocity value, U_∞, with an exponentially decreasing oscillation amplitude and a period that tends to some constant value. In contrast, when the plate inclination angle is smaller than the critical value, the bifurcation curve is monotonic and the velocity tends monotonically to U_∞. The solutions along these bifurcation curves are characterised by a foot-like structure that emerges from the meniscus and is preceded by a very thin precursor film further up the plate. The length of the foot increases continuously as one follows the bifurcation curve as it approaches U_∞. It is important to note that these solutions of diverging foot length do not converge to the Landau-Levich film solution at the same $U = U_\infty$. Indeed, the foot height at $U_\infty(\alpha)$ scales as $U^{1/2}$ while the Landau-Levich films scale as $U^{2/3}$. As expected, the results for the bifurcation curves that we here obtained with a precursor film model are similar to results obtained for such situations employing a slip model [5,12]. The protruding foot structure has been observed in experiments, *e.g.*, in refs. [5,6,15] where even an unstable part of the snaking curve was tracked. However, the particular transition described here has not yet been experimentally studied. This is in part due to the fact that in an experiment with a transversal extension (fully three-dimensional system) transversal meniscus and contact line instabilities set in before the foot length can diverge. We believe that experiments in transversally confined geometries may allow one to approach the transition more closely. Experiments with driving temperature gradients exist as well but focus on other aspects of the solution structure like, for instance, various types of advancing shocks (travelling fronts) and transversal instabilities [45]. We are not aware of studies of static foot-like structures in systems with temperature gradients.

We further note that the described monotonic and non-monotonic divergence of foot length with increasing plate velocity may be seen as a dynamic equivalent of the equilibrium emptying transition described in ref. [46]. There, a meniscus in a tilted slit capillary develops a tongue (or foot) along the lower wall. Its length diverges at a critical slit width. In our case, the length of the foot diverges at a critical plate speed —monotonically below and oscillatory above a critical inclination angle. The former case may be seen as a continuous dynamic emptying transition with a close equilibrium equivalent. The latter may be seen as a discontinuous dynamic emptying transition that has no analogue at equilibrium. This is further analysed in ref. [47].

Finally, we have shown that in an appropriate three-dimensional phase space, the three regions of the film profile, *i.e.*, the precursor film, the foot and the bath, correspond to three fixed points, $\boldsymbol{y}_p$, $\boldsymbol{y}_f$ and $\boldsymbol{y}_b$, respectively, of a suitable dynamical system. We have explained that the snaking behaviour of the bifurcation curves is caused by the existence of a heteroclinic chain that connects $\boldsymbol{y}_p$ with $\boldsymbol{y}_f$ and $\boldsymbol{y}_f$ with $\boldsymbol{y}_b$ at certain parameter values. We have proved a general result that implies that if the fixed points corresponding to the foot and to the bath have two-dimensional unstable and two-dimensional stable manifolds, respectively, and the fixed point corresponding to the foot is a saddle-focus so that the Jacobian at this point has the eigenvalues $-\lambda_1$, $\lambda_2 \pm \mathrm{i}\,\omega$, where $\lambda_{1,2}$ and ω are positive real numbers, then in the neighbourhood of the heteroclinic chain there is an infinite but countable number of heteroclinic orbits connecting the fixed point for the precursor film with the fixed point for the bath. These heteroclinic orbits correspond to solutions with feet of different lengths. Moreover, these solutions can be ordered so that the difference in the foot lengths tends to π/ω. We have also explained that in this case the bifurcation curve shows a snaking behaviour. Otherwise, if the fixed point corresponding to the foot is a saddle, the Jacobian at this point has three real non-zero eigenvalues, and the bifurcation curve is monotonic.

The presented study is by no means exhaustive. It has focused on obtaining asymptotic expansions of the solutions in the bath region using rigorous centre manifold theory and on analysing the collapsed heteroclinic snaking behaviour associated with the dragged meniscus problems. However, the system has a much richer solution structure. Beside the studied solutions one may obtain Landau-Levich films and investigate their coexistence with the discussed foot and mensicus solutions. For other solutions the bath connects directly to a precursor-type film which then connects to a thicker "foot-like" film which then goes back to the precursor-type film that continues along the drawn plate. These solutions and their relation to the ones studied here will be presented elsewhere.

The authors acknowledge several interesting discussions about the dragged film system with Edgar Knobloch, Serafim Kalliadasis, Andreas Münch, and Jacco Snoeijer, and about emptying and other unbinding transitions with Andy Parry and Andy Archer. This work was supported by the European Union under grant PITN-GA-2008-214919 (MULTIFLOW). The work of D.T. was partly supported by the EPSRC under grant EP/J001740/1. The authors are grateful to the Newton Institute in Cambridge, UK, for its hospitality during a brief common stay at the programme "Mathematical Modelling and Analysis of Complex Fluids and Active Media in Evolving Domains".

References

1. S.J. Weinstein, K.J. Ruschak, Annu. Rev. Fluid Mech. **36**, 29 (2004).
2. F.C. Morey, J. Res. Nat. Bur. Stand. **25**, 385 (1940).
3. J.J. Rossum, Appl. Sci. Res. Sect. A **7**, 121 (1958).
4. R.P. Spiers, C.V. Subbaraman, W.L. Wilkinson, Chem. Eng. Sci. **29**, 389 (1974).
5. J.H. Snoeijer, B. Andreotti, G. Delon, M. Fermigier, J. Fluid Mech. **579**, 63 (2007).
6. G. Delon, M. Fermigier, J.H. Snoeijer, B. Andreotti, J. Fluid Mech. **604**, 55 (2008).
7. M. Maleki, M. Reyssat, F. Restagno, D. Quéré, C. Clanet, J. Colloid Interface Sci. **354**, 359 (2011).
8. L. Landau, B. Levich, Acta Physicochim. U.R.S.S. **17**, (1942), reprint in [48].
9. P. Groenveld, Chem. Eng. Sci. **25**, 1259 (1970).
10. P. Groenveld, Chem. Eng. Sci. **25**, 1579 (1970).
11. S.D.R. Wilson, J. Eng. Math. **16**, 209 (1981).
12. J. Ziegler, J.H. Snoeijer, J. Eggers, Eur. Phys. J. ST **166**, 177 (2009).
13. E.S. Benilov, S.J. Chapman, J.B. McLeod, J.R. Ockendon, V.S. Zubkov, J. Fluid Mech. **663**, 53 (2010).
14. B. Jin, A. Acrivos, A. Münch, Phys. Fluids **17**, 103603 (2005).
15. J.H. Snoeijer, J. Ziegler, B. Andreotti, M. Fermigier, J. Eggers, Phys. Rev. Lett. **100**, 244502 (2008).
16. A. Münch, P.L. Evans, Physica D **209**, 164 (2005).
17. H. Riegler, K. Spratte, Thin Solid Films **210**, 9 (1992).
18. M.H. Köpf, S.V. Gurevich, R. Friedrich, L.F. Chi, Langmuir **26**, 10444 (2010).
19. M.H. Köpf, S.V. Gurevich, R. Friedrich, U. Thiele, New J. Phys. **14**, 023016 (2012).
20. U. Thiele, Adv. Colloid Interface Sci. **206**, 399 (2014).
21. L.P. Shilnikov, Sov. Math. Dokl. **6**, 163 (1965).
22. P. Glendinning, C. Sparrow, J. Stat. Phys. **35**, 645 (1984).
23. J. Knobloch, T. Wagenknecht, Physica D **206**, 82 (2005).
24. Y.P. Ma, J. Burke, E. Knobloch, Physica D **239**, 1867 (2010).
25. L.P. Shilnikov, Sov. Math. Dokl. **8**, 5458 (1967).
26. J. Knobloch, T. Wagenknecht, SIAM J. Appl. Dyn. Syst. **7**, 1397 (2008).
27. M. Chen, Appl. Anal. **75**, 213 (2000).
28. G.W. Hunt, M.A. Peletier, A.R. Champneys, P.D. Woods, M. Ahmer Wadee, C.J. Budd, G.J. Lord, Nonlinear Dyn. **21**, 3 (2000).
29. A. Oron, S.H. Davis, S.G. Bankoff, Rev. Mod. Phys. **69**, 931 (1997).
30. U. Thiele, Structure formation in thin liquid films. In S. Kalliadasis, U. Thiele (Editors), *Thin Films of Soft Matter*, (Springer, Wien, 2007) pp. 25–93.
31. P.-G. de Gennes, Rev. Mod. Phys. **57**, 827 (1985).
32. V.M. Starov, M.G. Velarde, J. Phys.: Condens. Matter **21**, 464121 (2009).
33. U. Thiele, J. Phys.: Condens. Matter **22**, 084019 (2010).
34. A.M. Cazabat, F. Heslot, S.M. Troian, P. Carles, Nature **346**, 824 (1990).
35. B. Scheid, E.A. van Nierop, H.A. Stone, Appl. Phys. Lett. **97**, 171906 (2010).
36. B. Scheid, E.A. van Nierop, H.A. Stone, Phys. Fluids **24**, 032107 (2012).
37. J. Carr, *Applications of Centre Manifold Theory*, Vol. **35** in *Applied Mathematical Sciences* (Springer-Verlag, Berlin, 1981).
38. I.U.A. Kuznetsov, *Elements of Applied Bifurcation Theory*, Vol. **112** in *Applied Mathematical Sciences* (Springer, New York, 1998).

39. E. Doedel, H.B. Keller, J.P. Kernevez, Int. J. Bifurcation Chaos Appl. Sci. Eng. **1**, 493 (1991).
40. E. Doedel, H.B. Keller, J.P. Kernevez, Int. J. Bifurcation Chaos Appl. Sci. Eng. **1**, 745 (1991).
41. H.A. Dijkstra, F.W. Wubs, A.K. Cliffe, E. Doedel, I.F. Dragomirescu, B. Eckhart, A.Y. Gelfgat, A. Hazel, V. Lucarini, A.G. Salinger, E.T. Phipps, J. Sanchez-Umbria, H. Schuttelaars, L.S. Tuckerman, U. Thiele, Commun. Comput. Phys. **15**, 1 (2014).
42. U. Thiele, L. Brusch, M. Bestehorn, M. Bär, Eur. Phys. J. E **11**, 255 (2003).
43. P. Beltrame, U. Thiele, SIAM J. Appl. Dyn. Syst. **9**, 484 (2010).
44. D. Tseluiko, J. Baxter, U. Thiele, IMA J. Appl. Math. **78**, 762 (2013).
45. A.L. Bertozzi, A. Münch, X. Fanton, A.M. Cazabat, Phys. Rev. Lett. **81**, 5169 (1998).
46. A.O. Parry, C. Rascon, E.A.G. Jamie, D.G.A.L. Aarts, Phys. Rev. Lett. **108**, 246101 (2012).
47. M. Galvagno, D. Tseluiko, H. Lopez, U. Thiele, Phys. Rev. Lett. **112**, 137803 (2014).
48. P. Pelce (Editor), *Dynamics of curved fronts*, 1st edition (Academic Press, London, 1988).
49. R.C. Robinson, *An introduction to dynamical systems: continuous and discrete* (Pearson Prentice Hall, Upper Saddle River, NJ, 2004).